Journal of Alloys and Compounds 1005 (2024) 176188

Contents lists available at ScienceDirect

Journal of Alloys and Compounds

journal homepage: www.elsevier.com/locate/jalcom

Superior energy storage performance of $Sr_{0.7}Bi_{0.2}TiO_3$-modified $Na_{0.5}Bi_{0.5}TiO_3$-$K_{0.7}La_{0.1}NbO_3$ lead-free ferroelectric ceramics

Xinyu Liu [a], Qin Li [a], Ting Wang [b], Weiping Gong [b,*], Taotao Ai [c], Yang He [a], Xinyu Chen [a], Minghui Hao [a], Minghui He [a], Meng Qi [a], Yuxiang He [a], Alexander N. Vtyurin [e], Chunlin Song [a,*], Gang Liu [a,c,d], Yan Yan [a,*]

[a] School of Materials and Energy, Southwest University, Chongqing 400715, China
[b] Guangdong Provincial Key Laboratory of Electronic Functional Materials and Devices, Huizhou University, Huizhou, Guangdong 516001, China
[c] School of Materials Science and Engineering, Shaanxi University of Technology, Hanzhong, Shaanxi 723001, China
[d] Chongqing Key Laboratory of Battery Materials and Technologies, Chongqing 400715, PR China
[e] Kirensky Institute of Physics SB RAS, Akademgorodok, Krasnoyarsk 660036, Russia

ARTICLE INFO

Keywords:
Energy storage performance
NBT
Relaxor ferroelectric ceramics
Polar nanoregions

ABSTRACT

$Na_{0.5}Bi_{0.5}TiO_3$ (NBT)-based ceramics exhibit significant potential as energy storage dielectric materials due to their high maximum polarization (P_{max}). However, their limited energy storage density significantly restricts their practical applications. To address this, this study optimizes the dielectric energy storage characteristics of lead-free relaxor ferroelectric ceramics based on $0.91Na_{0.5}Bi_{0.5}TiO_3$-0.09 $K_{0.7}La_{0.1}NbO_3$ (NBT-KLN) by incorporating $Sr_{0.7}Bi_{0.2}TiO_3$ (SBT) relaxor additives. The introduction of SBT helps maintain large polarization and induces local disorderly fields, promoting the formation of polar nanoregions. Subsequently, a viscous polymer processing (VPP) technique was employed to reduce defects and enhance density, markedly improving the breakdown strength (BDS). The findings indicate that the BDS of the optimized 0.30SBT (VPP) ceramics increased to 440 kV/cm, while achieving a high energy storage efficiency (η) of 78 % and an elevated energy storage density (W_{rec}) of 6.29 J/cm^3. Additionally, the 0.30SBT (VPP) ceramics demonstrate excellent temperature stability across a broad temperature range from 30 to 120 °C, making them ideal for long-term operation in variable environments. This study demonstrates superior results compared to previous research, thereby opening up new avenues for developing novel lead-free relaxor ferroelectric ceramics with superior energy storage characteristics.

1. Introduction

Ceramic dielectric capacitors have recently garnered significant research interest due to their high power density and superior reliability. However, the issue of low W_{rec} limits their application in advanced electronic system integration and miniaturization requirements [1,2]. To tackle this challenge, it is essential to design ceramic capacitors with high W_{rec}, high η, and excellent temperature stability. It is well known that the ideal W_{rec} and η depend on BDS and the polarization difference (ΔP) between maximum polarization (P_{max}) and remnant polarization (P_r) [3–5]. Therefore, high ΔP and large BDS are key factors in enhancing energy storage performance. In these aspects, relaxor ferroelectrics (RFE) show significant advantages over ferroelectrics (FE), antiferroelectrics (AFE), and linear dielectric (LD) due to their higher ΔP values and moderate BDS [1,6]. Although each of these materials has its own advantages and disadvantages in energy storage applications, RFEs demonstrate superior overall performance [7,8]. In recent years, $Na_{0.5}Bi_{0.5}TiO_3$ (NBT)-based RFE ceramics have shown good ferroelectric and dielectric properties at ambient temperature due to the similar 6 s^2 electron configuration of Bi^{3+} and Pb^{2+} [9,10].

However, pure NBT ceramics have a high P_r, which is detrimental to energy storage performance [11–13]. Studies have shown that doping NBT with $KNbO_3$ (KN) can disrupt the ferroelectric domain and induce polar nanoregions (PNRs) [14]. Additionally, KN is considered a ferroelectric material with significant spontaneous polarization similar to NBT [15]. Many researchers have utilized KN to dope and modify NBT ceramics, resulting in substantial improvements in their dielectric and piezoelectric properties [16]. For example, Wang et al. [14] introduced

* Corresponding authors.
E-mail addresses: gwp@hzu.edu.cn (W. Gong), chunlinsong@swu.edu.cn (C. Song), yanyan2013@swu.edu.cn (Y. Yan).

https://doi.org/10.1016/j.jallcom.2024.176188
Received 13 June 2024; Received in revised form 5 August 2024; Accepted 26 August 2024
Available online 27 August 2024

KN into NBT ceramics, resulting in NBT-KN ceramics with good energy storage characteristics and high P_{max}. However, due to the volatility of K_2O, it can lead to difficulties in controlling the stoichiometry and insufficient density of the ceramics during the sintering process. To address this issue, researchers often introduce lanthanide rare earth oxides into ceramics to regulate their structure and properties [17,18]. These rare earth oxides, by introducing specific chemical compositions and lattice defects, can optimize the density, breakdown strength, energy storage density, and other properties of NBT ceramics [19–21]. Liu et al. [22] chose to modify NBT-ST ceramics by doping them with La^{3+} to increase the density of the ceramics, achieving a high W_{rec} of 1.67 J/cm^3. Therefore, compensatively introducing the rare earth element La^{3+} into KN ceramics can form a solid solution $K_{0.7}La_{0.1}NbO_3$ to improve its sinterability. The synthesized NBT-KLN ceramics, serving as the research matrix for this experiment, further enhance their energy storage performance [23]. As an excellent linear relaxor ferroelectric ceramic, $Sr_{0.7}Bi_{0.2}TiO_3$ (SBT) can help improve ΔP and temperature stability in ceramics [24,25]. Therefore, many studies optimized energy storage performance by introducing SBT [26–29]. For example, Wang et al. [27] reported that NBT-*x*SBT relaxor ferroelectric ceramics exhibit a high P_{max} value at low electric fields. Additionally, their non-hysteretic *P-E* loops result in a high energy storage efficiency of up to 90 %. Chen et al. [30] selected SBTZ as a modifier to induce a phase transition in NBT ceramics, thereby enhancing their relaxor behavior. Among these, the 0.30SBTZ ceramic achieved a notable W_{rec} of 3.05 J/cm^3. Lv et al. [31] modified NBT-BT ceramics with SBT and Dy, effectively reducing remnant polarization and coercive field, resulting in a high W_{rec} of 4.87 J/cm^3 at room temperature.

Therefore, in this study, SBT was introduced into NBT-KLN ceramics to promote the formation of PNRs, ultimately enhancing their energy storage properties, as illustrated in Fig. 1(a1-a2). As the domain size decreases, PNRs can rapidly respond to electric fields [29]. This rapid response leads to a significant reduction in P_r and the coercive field (E_c) while also increasing BDS, as illustrated in Fig. 1(b1-b2). Furthermore, BDS is affected by several parameters, including the thickness of the ceramic, grain size, and porosity [20]. For instance, Wang et al. [32] utilized the viscous polymer processing (VPP) technique to fabricate NBT-SBT-BMS ceramics, achieving a BDS of 440 kV/cm. This ceramic not only has a W_{rec} of 7.5 J/cm^3 but also exhibits an η as high as 85 %. Therefore, by optimizing NBT-KLN-SBT ceramics using the VPP technique, significant enhancement in BDS is achieved, thereby endowing them with superior energy storage properties, as illustrated in Fig. 1 (b2-b3). The VPP technique involves repeatedly rolling and processing ceramic materials to create a more uniform and dense microstructure. This process not only effectively reduces the thickness of the ceramics but also significantly decreases internal defects, thereby greatly improving their electrical properties, as illustrated in Fig. 1(a3-a4) [31, 33].

In summary, the optimization of ceramics is progressively carried out following the path outlined in Fig. 1. Firstly, doping with SBT is

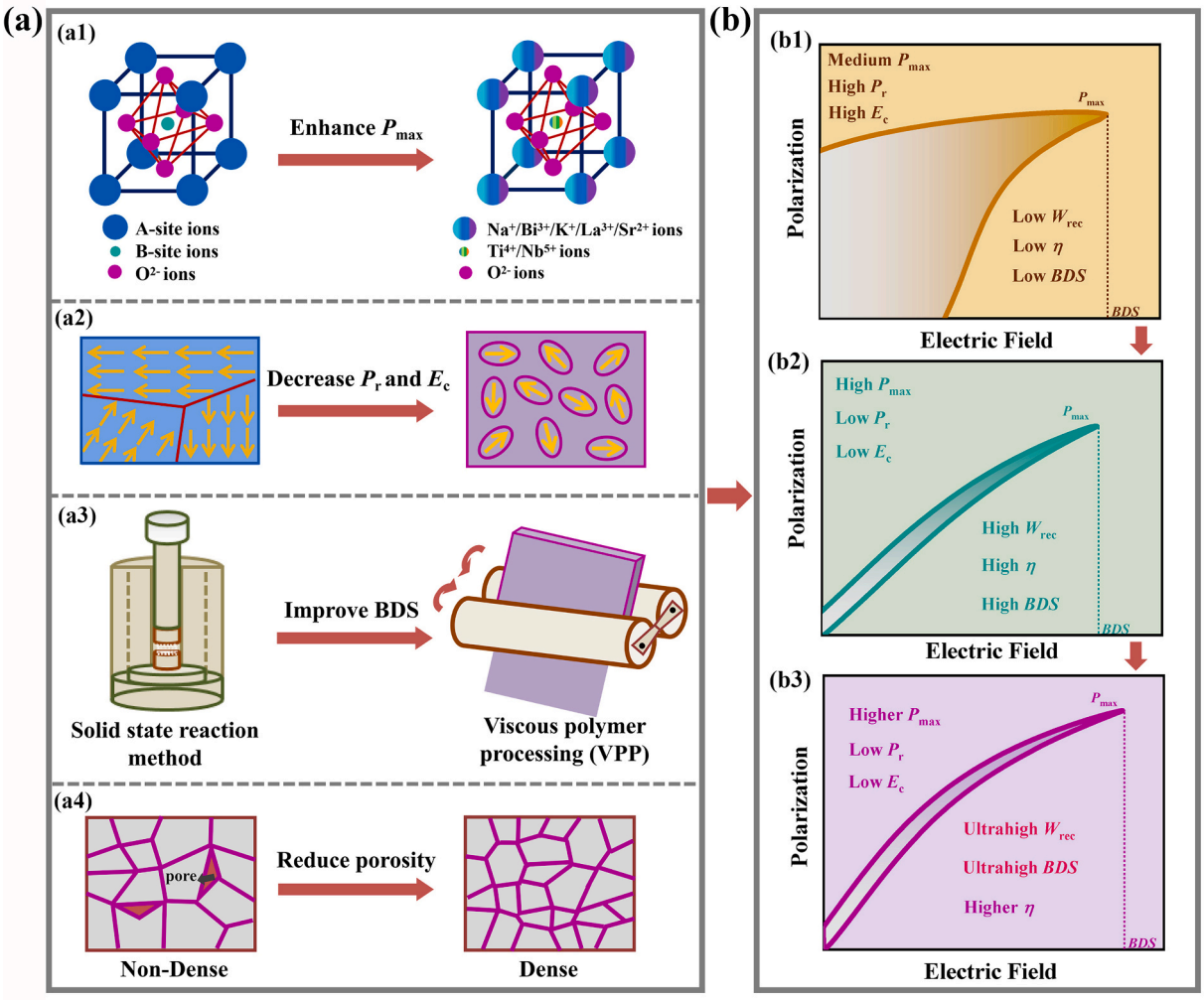

Fig. 1. A schematic illustration depicting the progressive enhancement of the energy storage properties of NBT-based ceramics via ion doping and process optimization.

introduced into NBT-KLN base ceramics to trigger the transformation of long-range ordered ferroelectric domains into PNRs, thereby reducing P_r and E_c. Subsequently, the resulting ceramics with optimal W_{rec} are further improved in BDS through the VPP technique, enhancing their energy storage performance. This study systematically investigated the electrical properties, microstructure, and domain structure of (1-*x*)(0.91$Na_{0.5}Bi_{0.5}TiO_3$-0.09 $K_{0.7}La_{0.1}NbO_3$)-*x*$Sr_{0.7}Bi_{0.2}TiO_3$ (NBT-KLN-*x*SBT) ceramics with *x* ranging from 0.10 to 0.40. The results demonstrate that this strategy is successful and holds promising prospects for application in ceramic dielectric capacitors.

2. Experimental

The lead-free ceramics (1-*x*)(0.91$Na_{0.5}Bi_{0.5}TiO_3$-0.09 $K_{0.7}La_{0.1}NbO_3$)-*x*$Sr_{0.7}Bi_{0.2}TiO_3$ (NBT-KLN-*x*SBT) were fabricated using traditional electro ceramic processing combined with die-pressing method. High-purity metal oxides or carbonates provided by Aladdin were used as raw materials, including Na_2CO_3 (99.8 %), K_2CO_3 (99 %), Bi_2O_3 (99 %), La_2O_3 (99.9 %), $SrCO_3$ (99.95 %), TiO_2 (99 %), and Nb_2O_5 (99.9 %). Weigh the required amounts according to the stoichiometric ratio. Mix anhydrous ethanol, zirconia balls, and powder evenly. After drying, the homogenized mixture was sintered at 900 ℃ for 3 hours and then subjected to another ball milling process. Subsequently, mix the blend with polyvinyl alcohol and press it into shape using a pressure of 10 MPa. Ultimately, sintering was conducted for 2 hours within the temperature ranging from 1190 to 1210 ℃. To continue improving the energy storage characteristics, the 0.30SBT composition was optimized using the VPP technique.

The NBT-KLN-*x*SBT samples were ground into fine powder and analyzed for their crystal structure using an X-ray diffractometer (Shimadzu, 6100). Use a Raman spectrometer (Horiba, LabRAM HR Evolution) to conduct Raman spectroscopy measurements. Use a scanning electron microscope (JEOL, JSM 6610) to observe the microstructure and employ an energy-dispersive X-ray spectrometer (EDS) to determine elemental distribution. During electrical measurements, the specimens were grounded down to 0.1 mm in thickness, and the upper and lower surfaces are coated with silver to serve as electrodes. Use an LCR meter (E4980AL, Keysight) to measure the dielectric and dielectric loss constant. Impedance spectroscopy data was measured using a high-temperature dielectric test system (Sanqi, 1210HTDE-LTC). *P-E* loops were performed using a ferroelectric analyzer (aixACCT, TF analyzer 2000E). The capacitors' charge-discharge characteristics were assessed with a dielectric charge-discharge testing system (TG Technology, CFD-003). The domain structure of the NBT-KLN-*x*SBT ceramics was imaged using a Piezoelectric force microscope (Asylum Research, MFP-3D), and domain evolution under electric fields was measured. TEM samples were prepared using a focused ion beam, and domain morphology was observed using a transmission electron microscope (TEM, JEOL-2200FS) with an acceleration voltage set to 200 kV.

3. Result and discussion

Fig. 2(a) shows the XRD spectra of NBT-KLN-*x*SBT ceramics at room temperature. It is evident that the 0.10SBT and 0.20SBT compositions exhibit a pure perovskite structure without any noticeable secondary phases. This indicates that SBT has fully integrated into the NBT-KLN matrix lattice, forming a single solid solution. However, with the increase in SBT doping content, trace secondary phase peaks were detected in the 0.30SBT and 0.40SBT compositions [34]. According to the standard PDF card, these secondary phases are identified as the $Bi_2Ti_2O_7$ phase (PDF: 00–032–0118). Magnifying the (200) diffraction peak near 46.5°, no signs of peak splitting were observed, suggesting that all samples possess a pseudocubic structure. Additionally, as the SBT doping level increases, the (200) diffraction peak gradually shifts towards lower angles [35,36]. The calculated tolerance factor (t) values (Table 1) indicate that this shift is due to the substitution of the larger ionic radius Sr^{2+} (1.44 Å) and Bi^{3+} (1.45 Å) for the smaller ionic radius La^{3+} (1.36 Å) and Na^{+} (1.39 Å) at the A site, leading to cell volume expansion and increased lattice parameters [37–40]. The Rietveld refinement of all compositions of the NBT-KLN-*x*SBT ceramics was performed using a mixed-phase model of *R*3c and *P*4bm, yielding detailed structural parameters as shown in Fig. 3(a)-(d). The R_{wp} values for all the ceramic compositions were less than 10 %, indicating that the refinement results are reliable. The tetragonal phase (*P*4bm) is usually considered a key factor in the relaxor behavior of NBT ceramics. The results show that with the increase in SBT content, the proportion of the *R*3c phase gradually decreases, while the proportion of the *P*4bm phase increases. This could be due to the strong ferroelectricity of the *R*3c phase ceramics under an electric field. As the SBT concentration increases, some long-range ferroelectric order is disrupted, indicating that SBT is an effective relaxor [41,42]. Notably, the appearance of the *F*d-3 m phase in the 0.30SBT and 0.40SBT ceramics might be due to the volatilization of Bi^{3+} during the sintering process, leading to uneven chemical reactions and the formation of a $Bi_2Ti_2O_7$ secondary phase, which corresponds to the scanning electron microscopy results.

To further investigation the structural evolution of NBT-KLN-*x*SBT

Table 1
The *t* of NBT-KLN-*x*SBT.

Ion	Site	$\lvert\Delta r/r\rvert$%	Tolerance factor (*t*)
Sr^{2+}	A	4.73	1.01
	B	136.07	0.71

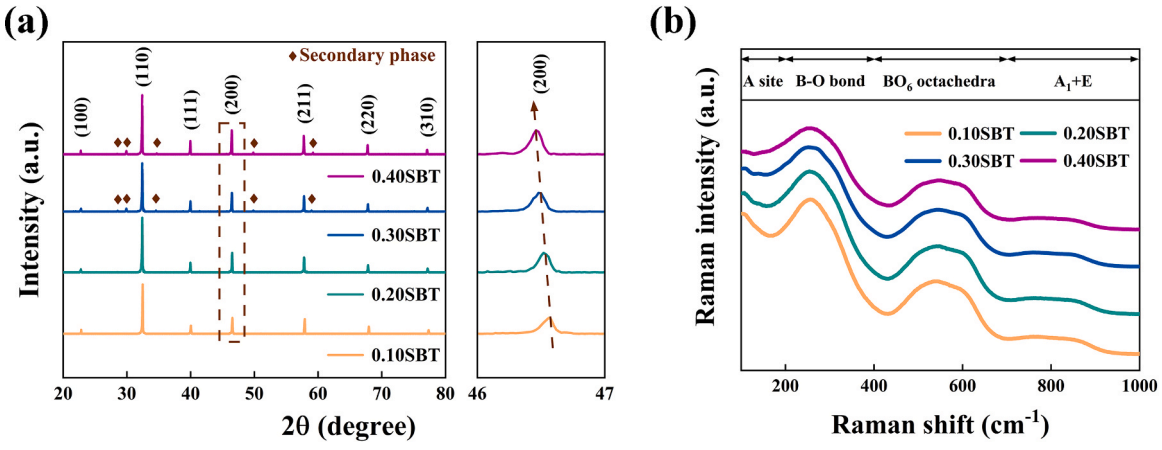

Fig. 2. (a) XRD pattern of NBT-KLN-*x*SBT ceramics. (b) Raman spectra for all ceramics.

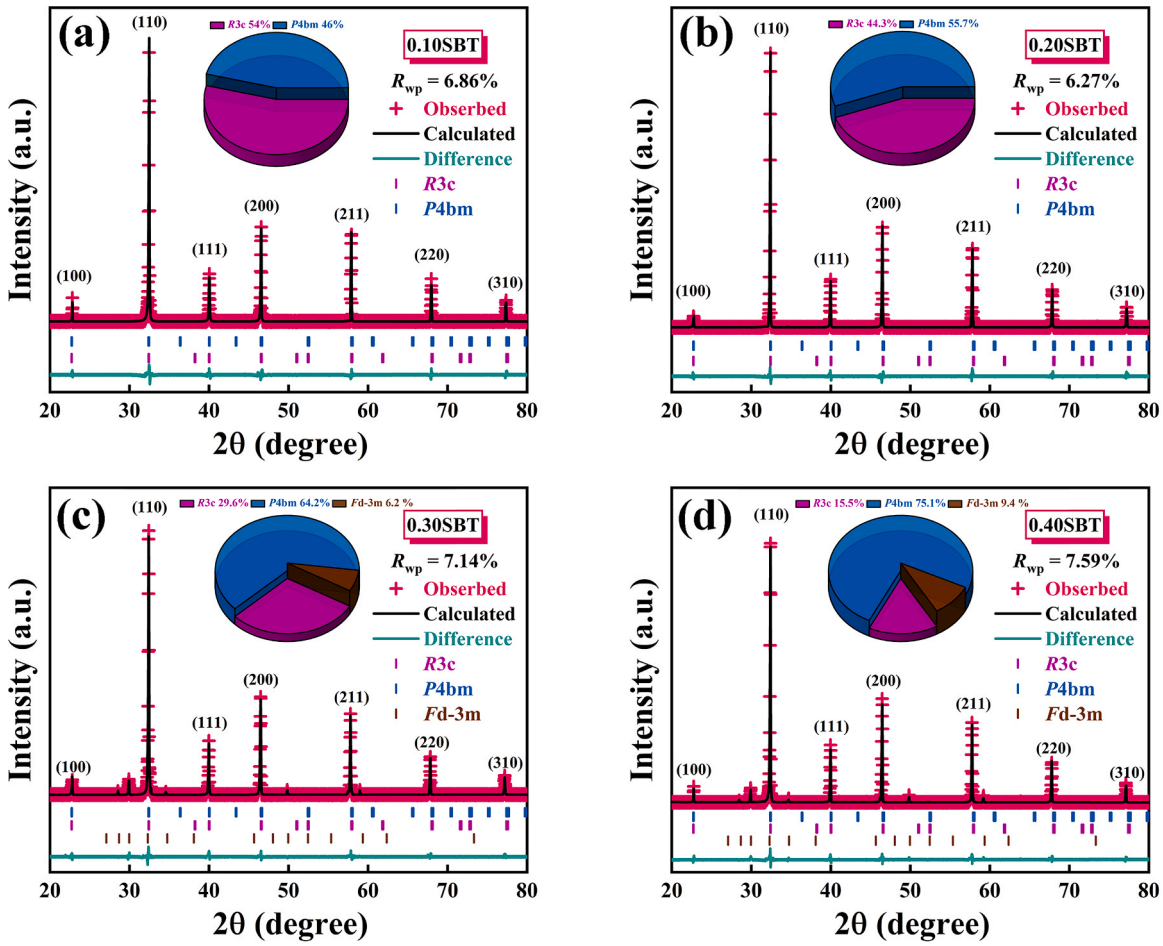

Fig. 3. (a)-(d) Rietveld refinement results of NBT-KLN-*x*SBT ceramics.

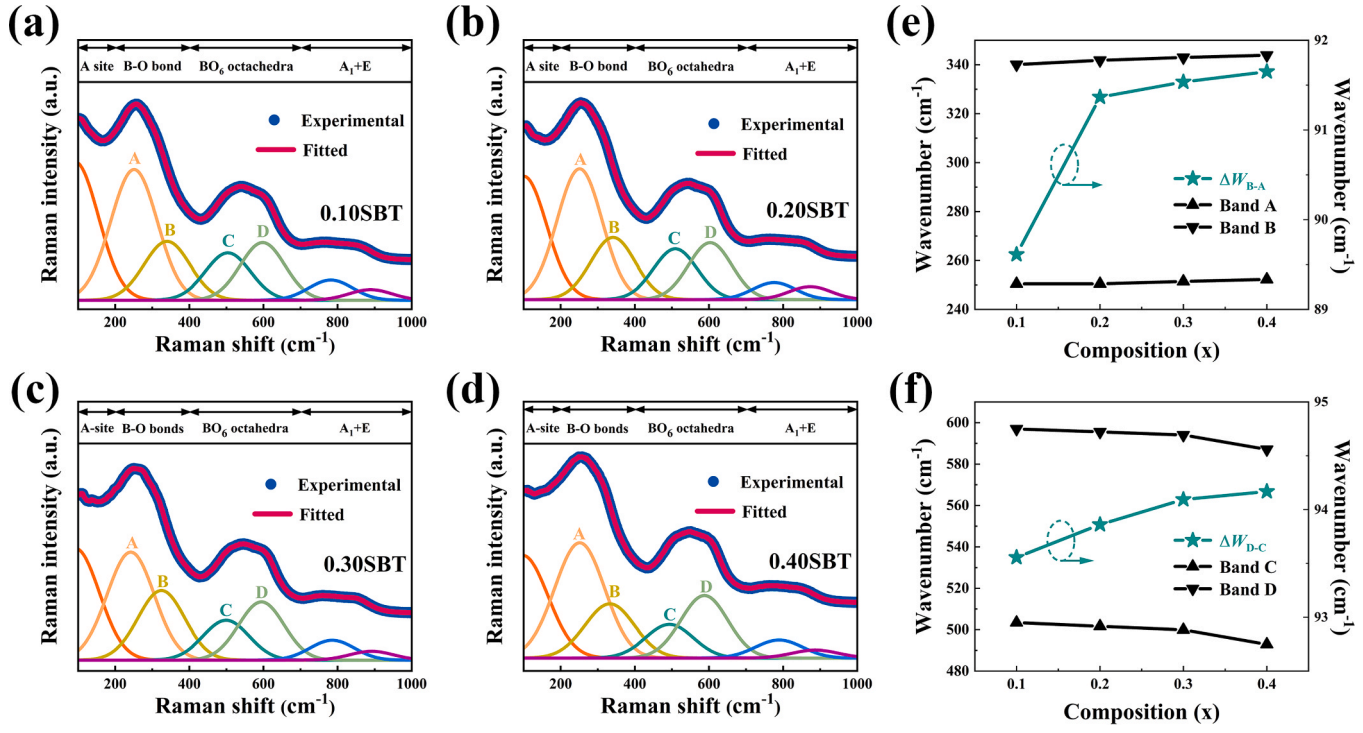

Fig. 4. (a)-(d) Raman spectra fitting results of NBT-KLN-*x*SBT ceramics. (e)-(f) Positions and differences of A, B, C, and D bands.

ceramics, Raman spectroscopy analysis was performed at ambient temperature, as illustrated in Fig. 2(b). Based on group theory analysis, NBT-based ceramics have 13 Raman active modes ($4A_1 + 9E$) for the rhombohedral (*R*3c) phase, 16 Raman active modes ($4A_1 + B_1 + 3B_2 + 8E$) for the tetragonal (*P*4bm) phase and no active modes for cubic (*P*m3m) phase [43–45]. Although previous Raman studies on NBT-based materials have shown that the number of experimental Raman modes is less than those of the theoretical Raman modes, these vibrational modes can be divided into the following four parts [46]: the vibrations of A-site ions ($Na^+/K^+/La^{3+}/Sr^{2+}/Bi^{3+}$-O) occur below 200 cm^{-1} [34], mainly involving A-O bonds. Vibrations in the 200–400 cm^{-1} range are related to B-O bonds (Ti^{4+}/Nb^{5+}-O). The 400–700 cm^{-1} range corresponds to the vibrations of the BO_6 octahedron, while the high-frequency region above 700–1000 cm^{-1} is characterized by overlapping bands of A_1 and E modes [47,48]. As the SBT doping level increases, the peaks associated with A-O and B-O bonds become broader, indicating an increase in ionic disorder and a weakening of long-range ferroelectric order [34]. Additionally, the valley-like features between the A-O and B-O bond vibration modes are related to lattice defects and internal stress [30,49,50].

Through further analysis of the Raman spectra, Fig. 4(a-d) presents the results after deconvolution based on Gaussian-Lorentzian modes. These include: (1) modes centered around 100 cm^{-1} related to vibrations of the perovskite A-site, (2) modes at 250 cm^{-1} and 340 cm^{-1} associated with B-O vibrations, (3) modes at 503 cm^{-1} and 597 cm^{-1} associated with BO_6 octahedral vibrations, (4) the region above 700 cm^{-1}, consisting of the last two modes associated with the overlapping bands of A_1 and E [11,29,46,51–53]. To observe the changes in the BO_6 octahedral vibrations and B-O band more clearly, Fig. 4(e) and (f) illustrate the precise peak positions for bands A, B, C, and D, along with the separations ($\Delta W_{B\text{-}A}$) between bands A and B, and ($\Delta W_{D\text{-}C}$) between bands C and D, which vary with the SBT content. The observation reveals that bands A and B shift towards higher wavenumbers, with $\Delta W_{B\text{-}A}$ gradually increasing, indicating an enhancement in relaxor characteristics. Furthermore, the expansion of $\Delta W_{D\text{-}C}$ suggests a decrease in crystal anisotropy. In conclusion, incorporating SBT not only increases the disorder at A and B sites but also significantly boosts the relaxor properties of the ceramics.

Fig. 5(a)-(d) show the surface microstructure of NBT-KLN-*x*SBT

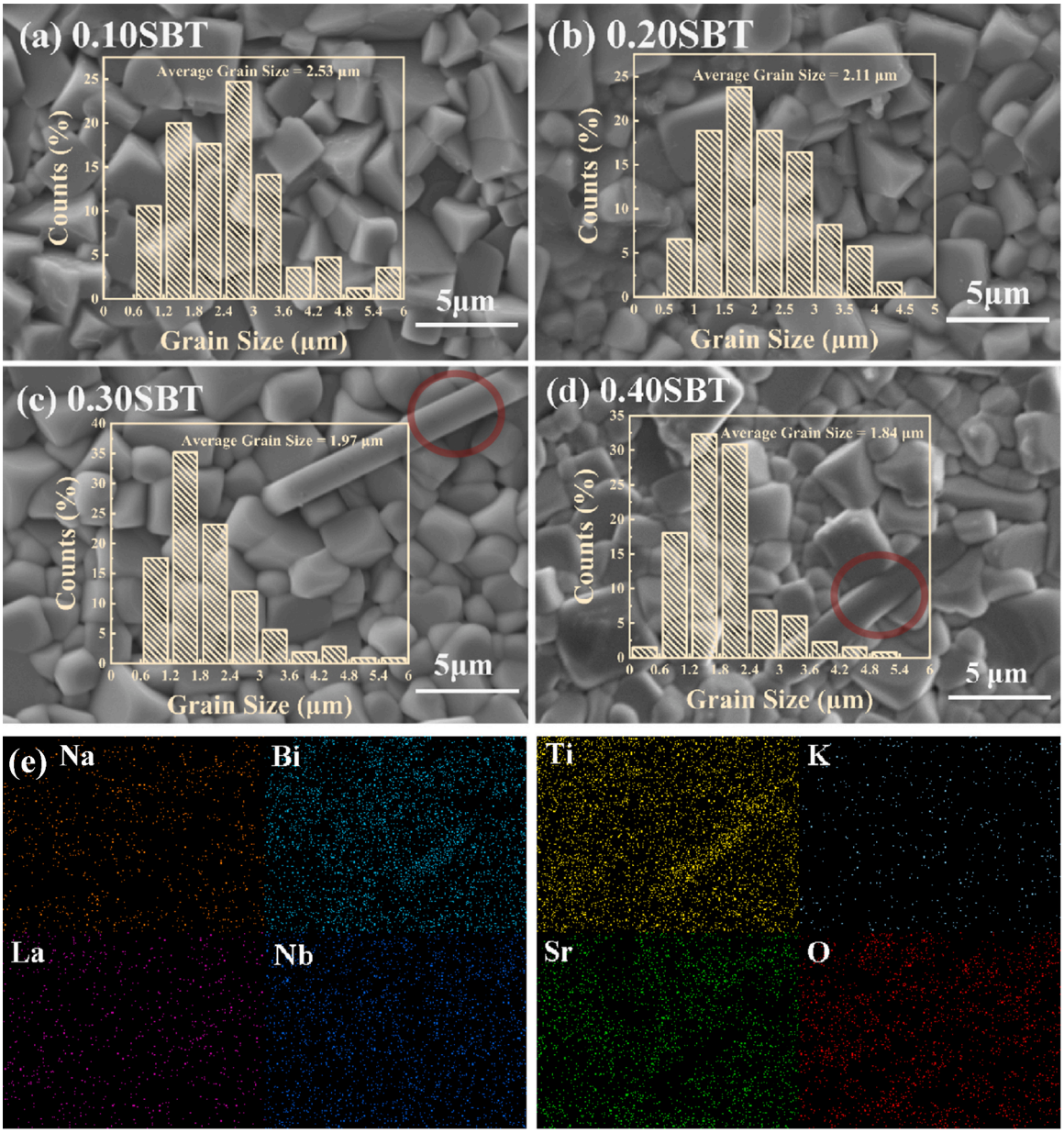

Fig. 5. (a)-(d) Surface SEM images of NBT-KLN-*x*SBT ceramics. (e) Elemental distribution of 0.40SBT ceramics.

ceramics. All compositions exhibit a uniform and dense microstructure, with distinct grain boundaries and low porosity. The average grain size (G_{avg}) was calculated using Nano-Measurement software, and with the specific results shown in the inset. With the increase in SBT doping level, the G_{avg} decreases monotonically from 2.53 μm to 1.84 μm. This likely occurs because of the entry of the larger ion radius of Sr^{2+} into the lattice A-site, leading to lattice rotation and deformation. The increase in lattice strain energy restrains grain growth by suppressing grain boundary activity [54,55]. Notably, rod-like secondary phases were observed in both 0.30SBT and 0.40SBT ceramics [13]. Additionally, the EDS results in Fig. 5(e) indicate that the rod-like secondary phases are enriched with Bi, Ti, and O, corresponding to the secondary phase $Bi_2Ti_2O_7$, which is consistent with the XRD results [54].

Fig. 6(a)-(d) depict the dielectric temperature spectra of NBT-KLN-*x*SBT ceramic samples. The dielectric spectra of all compositions exhibit two dielectric anomaly peaks, denoted as T_s and T_m [30]. Studies have shown that the random occupancy of different ions at the A-site or B-site may lead to the formation of numerous PNRs with varying potential barriers. Among them, T_s arises from the thermal evolution of *P*4bm and *R*3c polar nanoregions, corresponding to the ferroelectric-to-relaxor transition, while T_m arises from the thermal evolution of *P*4bm PNRs and their transition to *R*3c polar nanoregions [31,56]. Especially near T_s, a frequency dispersion phenomenon representing relaxor properties appears. This is due to the introduction of SBT, which increases the disorder of ions, breaks the ferroelectric domains, and enhances the relaxor behavior characteristic of short-range PNRs [57]. Additionally, with the increase in SBT doping level, the T_m representing the peak dielectric constant (ε_r) also shifts to lower temperatures. At the same time, the ε_r of the samples exhibits a decreasing trend, albeit with a small variation, which may be attributed to the relatively high dielectric constant of SBT [58]. At a frequency of 1 kHz, the dielectric constant varies by less than 15 % over the temperature range of 0 °C to 400 °C, indicating excellent high-temperature stability.

To investigate whether the insulation performance of NBT-KLN-*x*SBT ceramics is affected by electrode diffusion or by grains and grain boundaries, impedance spectroscopy tests were conducted over frequencies ranging from 20 Hz to 1 MHz and a temperature range of 500–580 °C. From Fig. 7(a)-(d), it can be noted that at each temperature point, the impedance spectra of all compositions exhibit a semicircular arc, indicating a similar conduction mode for all samples. As the temperature increases, the intersection of the semicircle representing the total resistance of the material with the real axis gradually decreases. This indicates that the resistance is influenced by temperature. Additionally, with the increase in SBT doping level, the diameter of the semicircular arc also increases. This implies that the electrical resistance increases with the increasing SBT doping level, optimizing the insulation performance. From the impedance imaginary part (-Z'') vs. frequency relationship shown in the top-right inset, it can be observed that the impedance spectra of all compositions consist of low-frequency peaks and high-frequency tails. These peaks appear in the mid-low-frequency region, indicating a significant influence of grain boundaries on the dielectric performance of the ceramics. The asymmetric broadening of the peaks suggests diffusion of relaxor times. As the temperature increases, the peaks gradually decrease in height and move to higher frequencies, indicating a decrease in relaxor time [20,59]. The shift in these peaks also indicates the presence of temperature-related dielectric relaxor and active conduction in response to grain boundaries. In the high-frequency region, the imaginary part of impedance curves overlap, demonstrating the release of space charge [60]. The impedance spectra at 500 ℃ were fitted using a parallel *R-C* equivalent circuit in Z-View to obtain reliable resistance values for the grains and grain boundaries. The results show that the fitting curve passes through all the data points, and the fitting results are satisfactory. The R_{gb} values for all samples are greater than the R_g values, indicating that the grain boundaries have good insulating properties. The resistances of the grains and grain boundaries follow the well-known thermally activated Arrhenius law, $\sigma = \sigma_0 \exp(-E_a/k_B T)$. Here, k_B and σ_0 represent the Boltzmann constant and the pre-exponential factor, respectively, and E_a is the activation energy. The calculated activation energy values for NBT-KLN-*x*SBT ceramics are shown in Fig. 7(e). The activation energy E_a monotonically increases

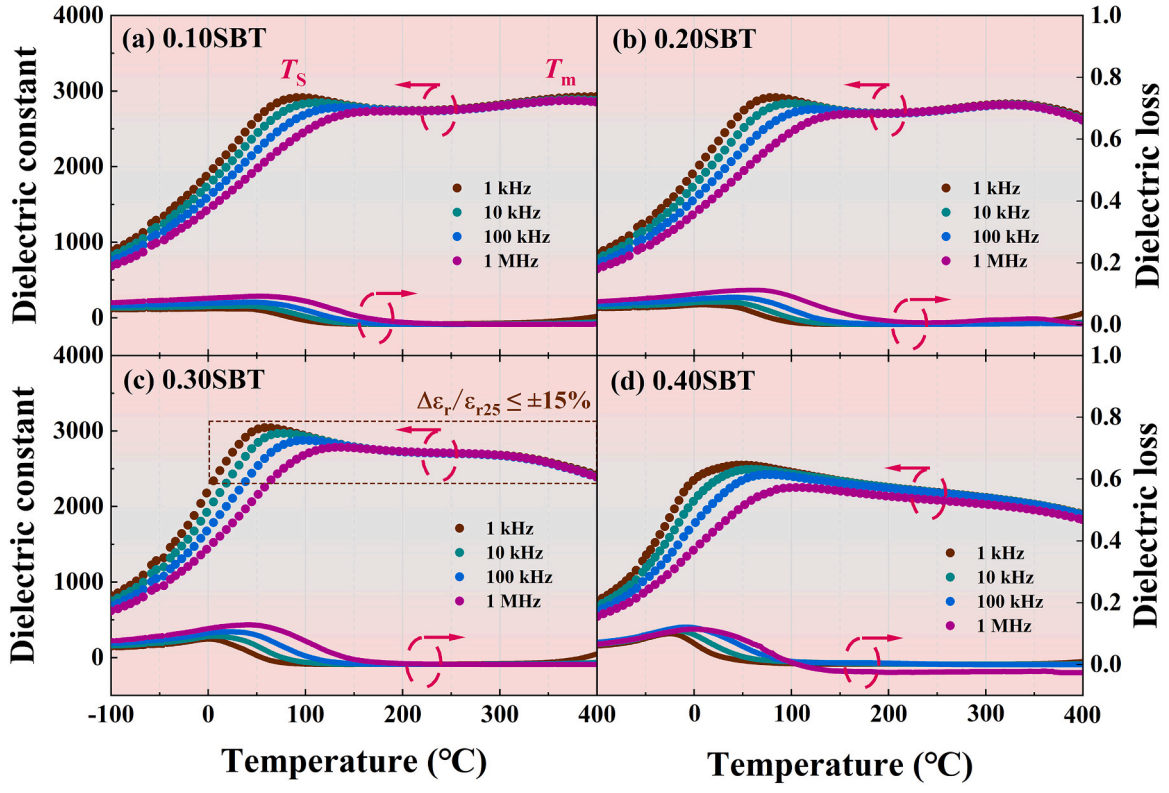

Fig. 6. The dielectric performance of NBT-KLN-*x*SBT ceramics.

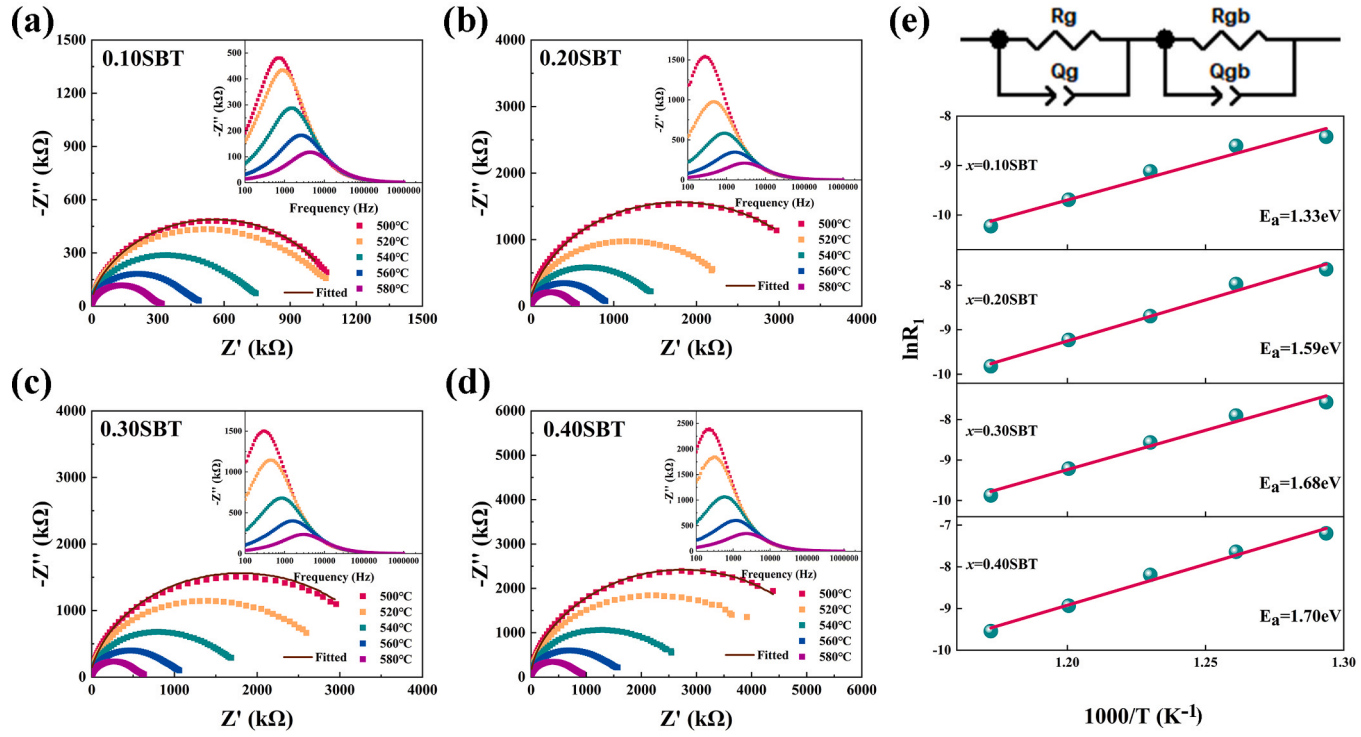

Fig. 7. (a)-(d) Complex impedance plots of NBT-KLN-*x*SBT ceramics. (e) Arrhenius plots of the impedance.

with increasing SBT content, indicating an enhanced ability to impede long-range electron movement, as higher electron transition barriers require more energy. This also implies a lower defect concentration in the ceramics, resulting in reduced leakage current [61,62].

The *P-E* curves of NBT-KLN-*x*SBT ceramics measured at 10 Hz are depicted in Fig. 8(a)-(d). Clearly, with the increase in SBT concentration, the *P-E* curves become progressively narrower, and P_r decreases sharply. This indicates that the long-range ordered ferroelectric domains are being disrupted and gradually transformed into PNRs, resulting in more pronounced relaxor behavior in the ceramics. Specifically, at 200 kV/cm, the changes in P_r are as follows: 7.84, 4.67, 3.77, and 3.70 μC/cm^2, while P_{max} slightly decreases from 39.93 μC/cm^2 to 36.91 μC/cm^2. The calculated ΔP ($\Delta P = P_{max} - P_r$) exhibits a pattern of initially increasing and then decreasing, reaching its peak value of 34.35 μC/cm^2 in the 0.30SBT ceramic. Thus, the 0.30SBT ceramic has been chosen as the representative sample for in-depth analysis. Fig. 8(e) depicts the *P-E* loops of the 0.30SBT ceramic at varying electric field strengths. The *P-E* loops clearly exhibit saturated polarization characteristics, which can be

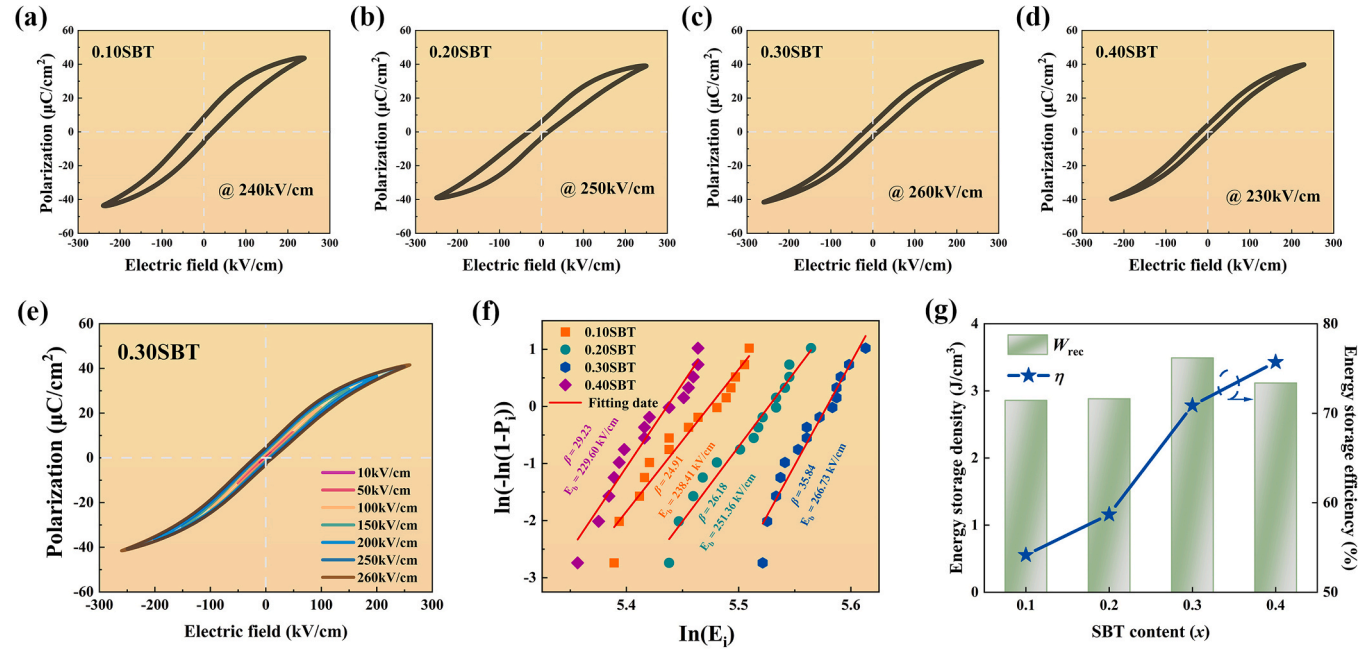

Fig. 8. (a)-(d) *P-E* curves of NBT-KLN-*x*SBT ceramics. (e) *P-E* loops of NBT-KLN-0.30SBT ceramics under various electric fields. (f) Weibull distributions of NBT-KLN-*x*SBT ceramics. (g) Energy storage performance.

attributed to the incorporation of the SBT relaxor and the existence of nanodomains. As depicted in Fig. 8(g), the η rises with the SBT doping content. This is because the long-range ordered ferroelectric macro-domains in the ceramic samples are disrupted, leading to enhanced relaxor behavior, which contributes positively to enhancing energy storage properties. Specifically, the 0.30SBT ceramic achieved a high P_{max} of 41.55 μC/cm^2 at 260 kV/cm, resulting in an η of 71 % and an W_{rec} of 3.49 J/cm^3. It is well known that the BDS of dielectrics is a key characteristic for evaluating material performance. All data in Fig. 8(f) follow a Weibull distribution, and the calculated BDS values for the ceramic samples are 238, 251, 266, and 229 kV/cm, respectively. The proximity of these values to those acquired through *P-E* loop tests underscores the reliability of BDS measurements within the context of *P-E* loop tests.

To further investigate the domain structure of NBT-KLN-0.30SBT ceramics and preliminarily determine their crystal structure, representative grains were characterized by TEM. Fig. 9(a) shows the bright-field image of the ceramic sample. The wedge and lamellar shaped domains are observed simultaneously, corresponding respectively to the rhombohedral and tetragonal phase regions [63,64]. Additionally, the HRTEM image in Fig. 9(d) reveals excellent crystal quality. Measurements from the fast Fourier transform (FFT) and inverse fast Fourier transform (IFFT) indicate that the lattice spacing of the [111] axis (d = 0.27 nm) is consistent with a pseudocubic structure [65,66]. The superstructure reflections observed in the selected area electron diffraction (SAED) patterns can be used to easily determine the symmetry of the structure. Fig. 9(b-c) show the SAED patterns of the wedge-shaped domains, while Fig. 9(e-f) display those of the lamellar domains. The presence or absence of superstructure reflections caused by octahedral tilting is a useful indicator for identifying different space groups and crystal structures. In the *R*3c phase, 3-axis anti-phase tilting represented by $a^-a^-a^-$ Glazer notation results in 1/2{*ooo*} type superstructure reflections. The *P*4bm phase with single-axis in-phase tilting denoted as $a^0a^0c^+$ leads to 1/2{*ooe*} type superstructure reflections, where *o* and *e* correspond to odd and even Miller indices [45,67]. The observation of 1/2{*ooo*} superstructure reflections along the [110] axis, but not along the [111] axis, indicates the presence of the *R*3c phase, based on the presence of 1/2{*ooo*} and the absence of 1/2{*ooe*} superstructure reflections. Similarly, the presence of 1/2{*ooe*} superstructure reflections along the [001] and [111] axes indicates the existence of the *P*4bm symmetry phase. This discussion confirms the coexistence of *R*3c and *P*4bm mixed phases in the NBT-KLN-0.30SBT ceramics, consistent with the XRD refinement results.

Numerous studies have shown that Piezoelectric force microscope (PFM) is a very effective method for observing changes in domain structures. To gain deeper insights into the fundamental mechanisms driving the superior energy storage properties of 0.30SBT ceramics, PFM was used to observe the domain structure changes in 0.10SBT and 0.30SBT ceramics, including height, amplitude, and phase modes. As shown in Fig. 10, the surface morphology of the ceramics is smooth, with a height variation within 5 nm. The black and yellow areas represent polarization directions opposite to and the same as the applied electric field, respectively. In the 0.10SBT ceramic, large block-shaped domains and a few nearby nano-domains can be observed. With the increase in SBT, the size of the block-shaped domains in the 0.30SBT ceramic decreases and transforms into a large number of dispersed PNRs. This change in domain size is believed to be due to the disruption of the long-range ferroelectric order of the A-site or B-site structure with the addition of SBT, enhancing the relaxor properties of the ceramic. Generally, smaller domains or PNRs exhibit high dynamics, resulting in higher relaxor behavior and lower energy barriers, allowing them to respond quickly under an electric field. This characteristic leads to a high W_{rec} while effectively reducing the P_r, thus giving the 0.30SBT ceramic excellent energy storage performance. This phenomenon is consistent with the *P-E* curve results shown in Fig. 8(e).

Traditional die-pressing methods often fail to achieve high densification in energy storage ceramics. As a result, 0.30SBT ceramics exhibit a high P_{max} but low η. To address this issue, we used the VPP technology

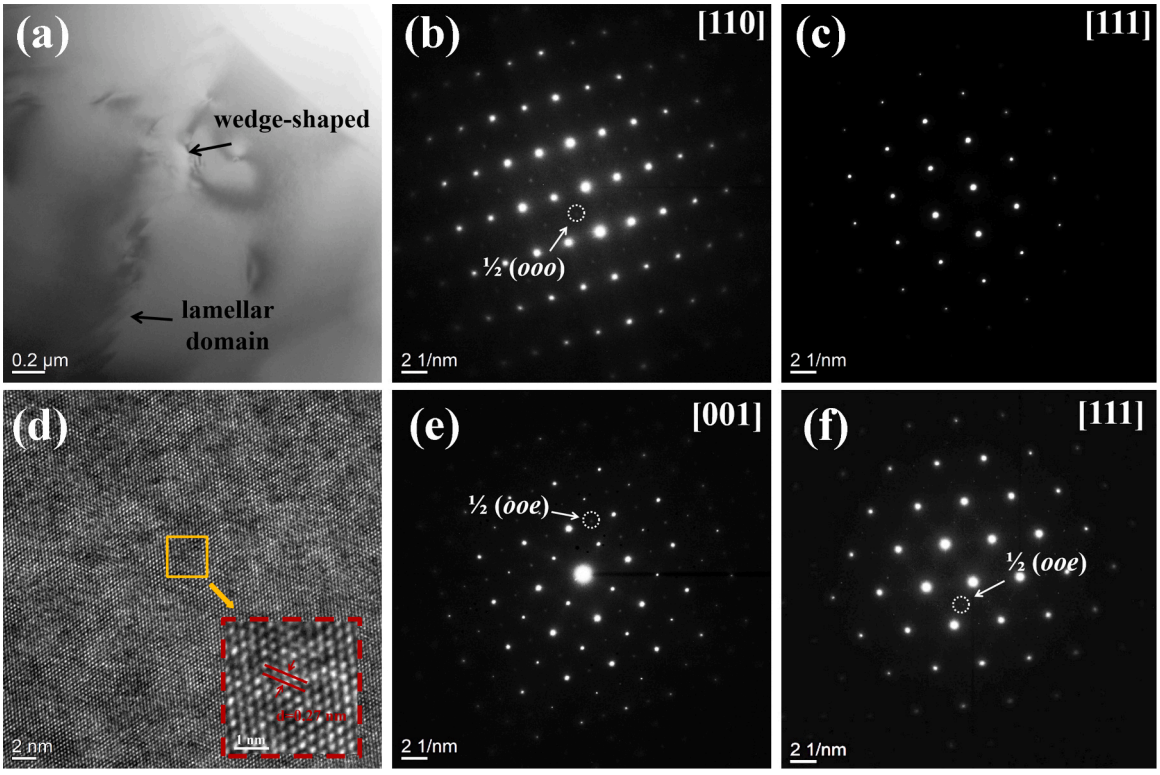

Fig. 9. TEM image of NBT-KLN-0.30SBT ceramics. (a) Bright-field images of grains. (d) HRTEM images. SAED patterns along (b) [110], (e) [001] and (c, f) [111] zone axes.

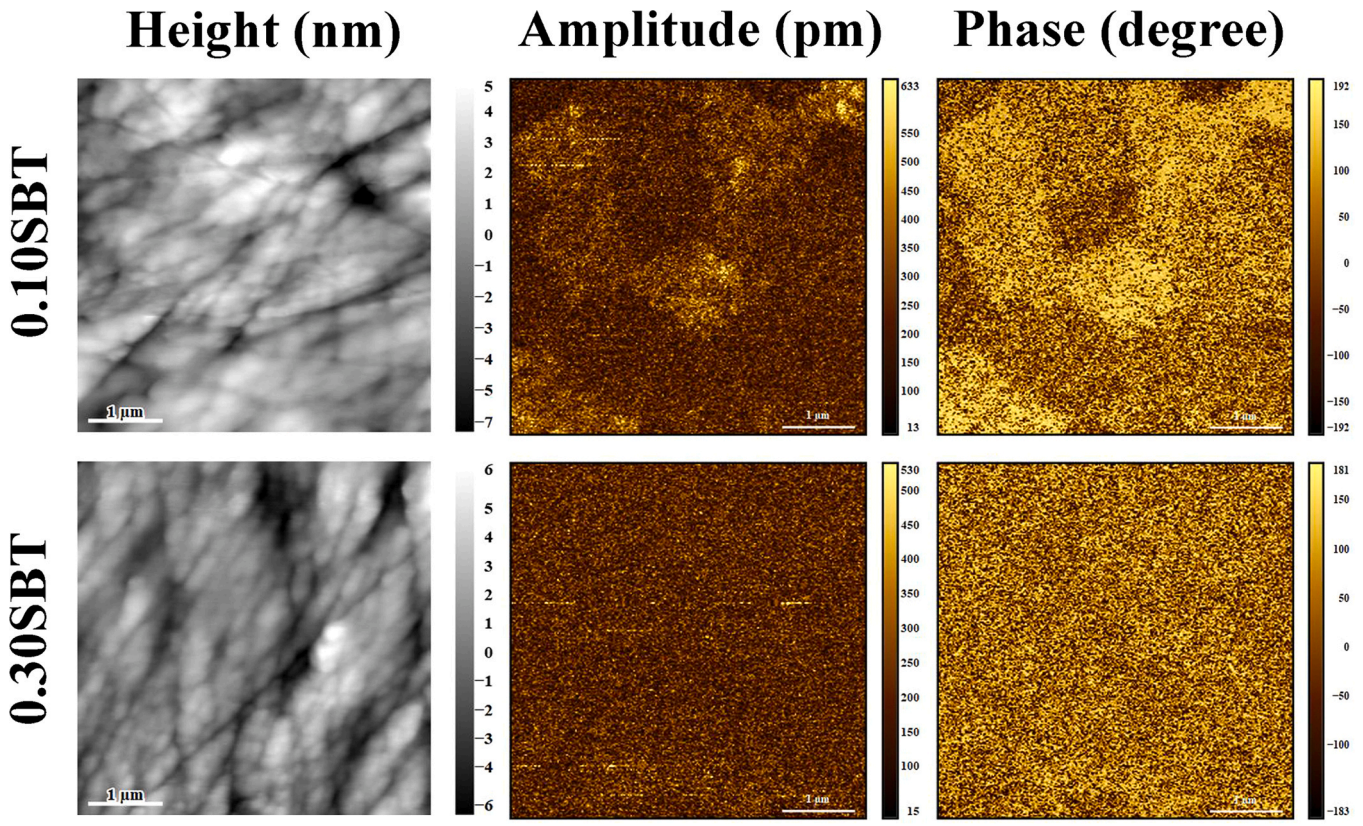

Fig. 10. PFM images of NBT-KLN-*x*SBT ceramics.

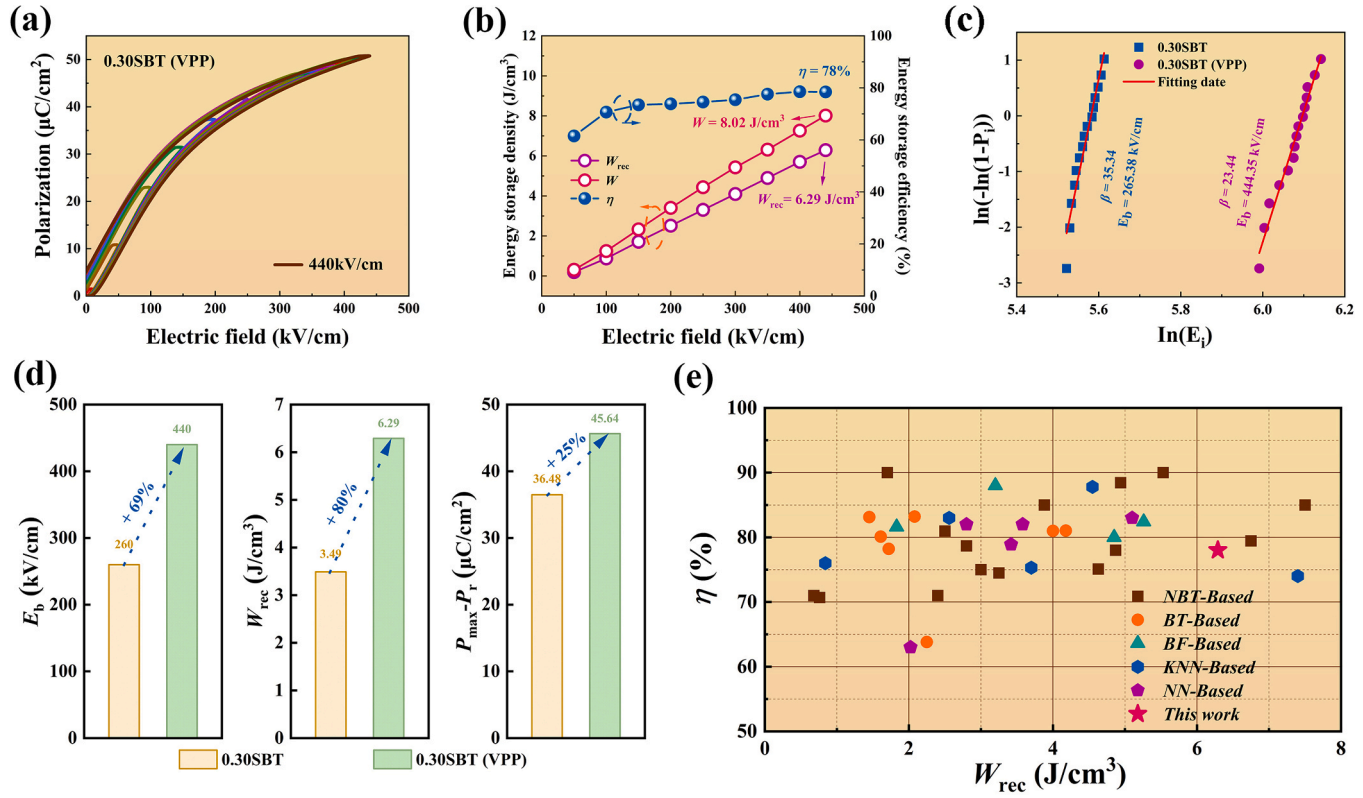

Fig. 11. (a) *P-E* curves of 0.30SBT (VPP) ceramics and (b) energy storage performance. (c) Weibull distributions of 0.30SBT (VPP) ceramics. (d) Energy storage performance comparison between 0.30SBT (VPP) and 0.30SBT ceramics (e) Comparison of W_{rec} and η between lead-free ceramics in this study and those in other literature.

to fabricate 0.30SBT ceramic thin sheets. This method aims to eliminate the limitations of traditional die-pressing techniques in achieving high BDS. Fig. 11 illustrates the room-temperature *P-E* curves and energy storage characteristics of the optimized 0.30SBT ceramics fabricated using the VPP technique. It is evident from Fig. 11(a) that the BDS increased from 260 kV/cm to 440 kV/cm, indicating that the VPP technique is an effective approach to improve the BDS of ceramics. As depicted in Fig. 11(b), the W_{rec} of the 0.30SBT (VPP) ceramics reached 6.29 J/cm^3, which is 1.8 times greater than that of the 0.30SBT ceramics prepared using traditional die-pressing methods. Additionally, its η increased to 78 %, indicating a substantial enhancement in the comprehensive energy storage performance. The comparison of Weibull distributions in Fig. 11(c) between the 0.30SBT ceramics and the 0.30SBT (VPP) ceramics further confirms that the VPP technique significantly improves the BDS of dielectric ceramics. This improvement is mainly due to the VPP technique reducing the thickness of the ceramics and decreasing defects such as porosity, thereby achieving higher BDS and P_{max}. Fig. 11(d) illustrates the changes in three key parameters, namely BDS, W_{rec}, and P_{max}-P_r, of the 0.30SBT ceramics before and after VPP. The VPP technique increased the BDS of the 0.30SBT ceramics by 69 % from 260 kV/cm to 440 kV/cm, elevated P_{max}-P_r by 25 % from 36.48 μC/cm^2 to 45.46 μC/cm^2, and ultimately achieved a substantial increase in W_{rec} from 3.49 J/cm^3 to 6.29 J/cm^3, representing an 80 % improvement. This enhancement is primarily attributed to the overall improvement in BDS and P_{max}-P_r. Fig. 11(e) and Table 2 present a comparison of the efficiency and effective density of 0.30SBT (VPP) ceramics with other lead-free energy storage ceramics, indicating its outstanding comprehensive energy storage performance [11,20,23–25,31,32,39,40,68–104].

Investigating the performance stability of 0.30SBT (VPP) ceramics under different frequencies and temperature conditions is crucial. This can clarify the optimal operating temperature range and applicable frequency range of the sample, providing important references for the application and research of subsequent electronic devices [105]. Fig. 12 (a-b) shows the variation of the single-pole *P-E* curves of 0.30SBT (VPP) ceramics within the frequency range of 1–80 Hz, and calculates and statistically analyzes the changes in P_{max}, P_r, W_{rec}, and η. It can be observed that, at 250 kV/cm, as the frequency increases, the P_{max} of 0.30SBT (VPP) ceramics slightly decreases from 41.57 μC/cm^2 to 40.10 μC/cm^2, with a variation rate of less than 0.02 %. Meanwhile, P_r shows a trend of gradual increase. Simultaneously, the *P-E* curves progressively widen, η remains above 61 %, W_{rec} is above 2.91 J/cm^3, indicating its good frequency stability. Fig. 12(c) shows the *P-E* loops of 0.30SBT (VPP) ceramics at 250 kV/cm, at temperatures from 30 to 120 °C. It can be clearly seen that the overall shape of the *P-E* loops is relatively narrow. Analyzing Fig. 12(d) alongside reveals that as the temperature rises, the change in P_{max} remains minimal, whereas P_r shows a slight increase, ranging from 39.93 to 37.81 μC/cm^2 and from 3.85 to 4.61 μC/cm^2, with variation rates of 5.30 % and 19.74 %, respectively. W_{rec} and η remain above 2.92 J/cm^3 and 71 %, respectively, with fluctuations of less than 8.80 % and 4.10 %. This indicates that 0.30SBT (VPP) ceramics exhibit good temperature stability, which is beneficial for stable operation under different temperature conditions.

Fig. 13(a) displays the over-damped pulse discharge current waveform of 0.30SBT (VPP) ceramics at ambient temperature. The tested voltage rises from 50 kV/cm to 250 kV/cm in steps of 50 kV/cm. One can note that the current rapidly reaches its maximum value within a brief timeframe. The corresponding discharge energy density (W_{dis}) versus time relationship curves are shown in Fig. 13(b), where W_{dis} increases to 4.00 J/cm^3 at 250 kV/cm. Furthermore, W_{dis} achieves its peak rapidly, taking only 137 ns (as indicated by $t_{0.9}$, which confirms discharge speed by representing the time needed for a dielectric energy storage ceramic capacitor to reach 90 % of total discharge energy), showcasing its significant capability for quick pulse power applications. Fig. 13(c) shows the under-damped discharge curve of 0.30SBT (VPP) ceramics. Combined with Fig. 13(d), it is evident that the power density (P_D), current density (C_D), and peak current (I_{max}) all increase with the increase in electric field, reaching their respective maximum values at 250 kV/cm: 31.20 A, 138.05 MW/cm^3, and 1104.42 A/cm^2. The high C_D of the ceramic can be associated with its abbreviated discharge time and elevated induced polarization [106]. These results reveal that 0.30SBT (VPP) ceramics have broad prospects in pulse power technology.

Similarly, to analyze the temperature suitability of 0.30SBT (VPP) ceramics, the pulse performance test results under varying temperature conditions (30–120 ℃, 250 kV/cm) are depicted in Fig. 14. The variation range of W_{dis} is from 3.03 to 3.34 J/cm^3, with a variation rate of 10 %, reaching its maximum value at 90 °C. C_D varies from 1090.27 to 1203.54 A/cm^2, while P_D ranges from 136.28 to 150.44 MW/cm^3. These results demonstrate that 0.30SBT (VPP) ceramics exhibit excellent and temperature-stable pulse performance.

Table 2
Comparison of W_{rec} and η of energy storage ceramics.

Composition	W_{rec}(J/cm^3)	η(%)	E (kV/cm)	Reference
0.5(Bi0.9Dy0.1)FeO3−0.5BaTiO3	3.6	75	175	[98]
90BNBT−10AN	3.92	53	180	[99]
0.55(Bi0.7Nd0.3)FeO3−0.45BT	2.11	89	170	[100]
0.7(Bi0.85Gd0.15)FeO3−0.3BT	6.5	48.5	260	[101]
BF-BT−0.14AN	2.11	84	195	[102]
BF-BT−0.15NN	8.2	70	300	[103]
$(Bi_{0.7}Ba_{0.3})_{0.8}Na_{0.2}(Fe_{0.7}Ti_{0.3})_{0.8}Ta_{0.2}O_3$	10.3	68	550	[104]
0.94SBT−0.06(KB)(MNb)	2.6	88	280	[25]
0.94SBT−0.06BMC	1.67	90	240	[24]
0.7BT−0.3(SBT-BMT)	1.12	94	170	[39]
NKBBT−0.3CST	2.39	75	220	[40]
0.90(NBT-ST)−0.10BNN	4.1	83	250	[92]
NBT-SBT−0.04ACN	4.6	82	260	[93]
BSZT−0.5NBT	4.45	95	360	[94]
BNT-SBT−4NN	3.08	81	220	[95]
NBT-SBT−6.5SGNVPP	5.2	85	350	[96]
NBT-KLN−0.10BMTVPP	6.7	82	440	[23]
BF-BT−0.12NT MLCCs	9.1	80	780	[97]
NBT-KLN−0.30SBTVPP	6.29	78	440	This work

4. Conclusions

In summary, this paper conducted a multi-angle analysis of NBT-KLN-*x*SBT ceramics focusing on domain structure modulation, including microscopic structure, energy storage performance, and domain structure. Additionally, to further enhance the comprehensive energy storage characteristics, 0.30SBT (VPP) ceramics were prepared through the VPP technique. The research results indicate that incorporating SBT can disrupt the long-range ordered state of ferroelectric domains, resulting in a reduction in domain size while the forming numerous PNRs, thereby enhancing the ceramic's relaxor characteristics. Additionally, the *P-E* curves progressively narrow with the increase in SBT concentration, resulting in a sharp decrease in P_r and a significant improvement in energy storage characteristics. Among these, 0.30SBT ceramics achieved a BDS of 260 kV/cm, with P_{max} remaining at 41.55 μC/cm^2, yielding an η of 71 % and an W_{rec} of 3.49 J/cm^3. The energy storage characteristics of the optimized 0.30SBT (VPP) ceramics after the VPP technique has been significantly enhanced. Its BDS has risen from 260 to 440 kV/cm, while W_{rec} has reached 6.29 J/cm^3, and the η improved to 78 %. Moreover, both its energy storage performance and pulse performance demonstrate good temperature stability (30–120 °C). Additionally, at ambient temperature with an electric field of 250 kV/cm, its $t_{0.9}$ is 137 ns, and P_D and C_D reach 138.05 MW/cm^3 and 1104.42 A/cm^2, respectively. Under varying temperature conditions, P_D remains stable at 136.28 MW/cm^3 or higher. These characteristics substantiate the substantial application potential of 0.30SBT (VPP) ceramics in pulse power capacitors. By using TEM, the energy storage performance enhancement mechanism of

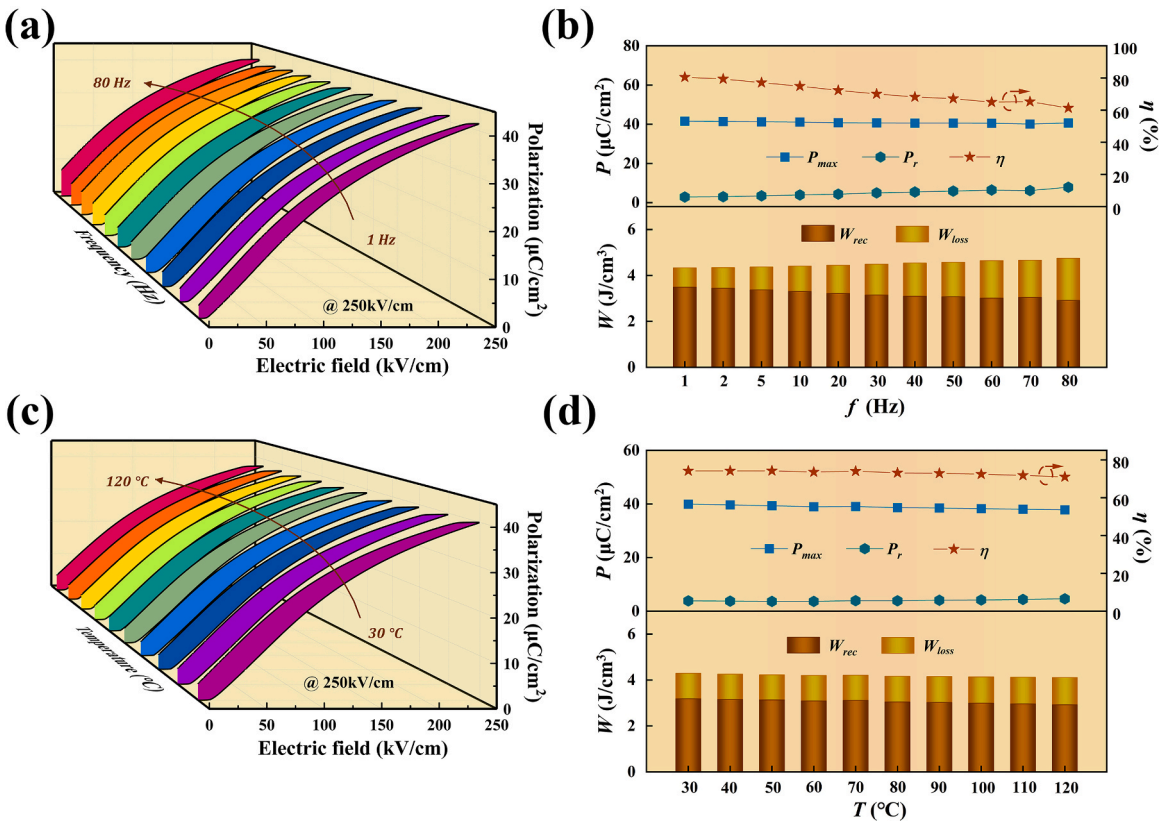

Fig. 12. (a)-(b) Frequency-dependent and (c)-(d) temperature-dependent *P-E* curves and energy storage characteristics of 0.30SBT (VPP) ceramics.

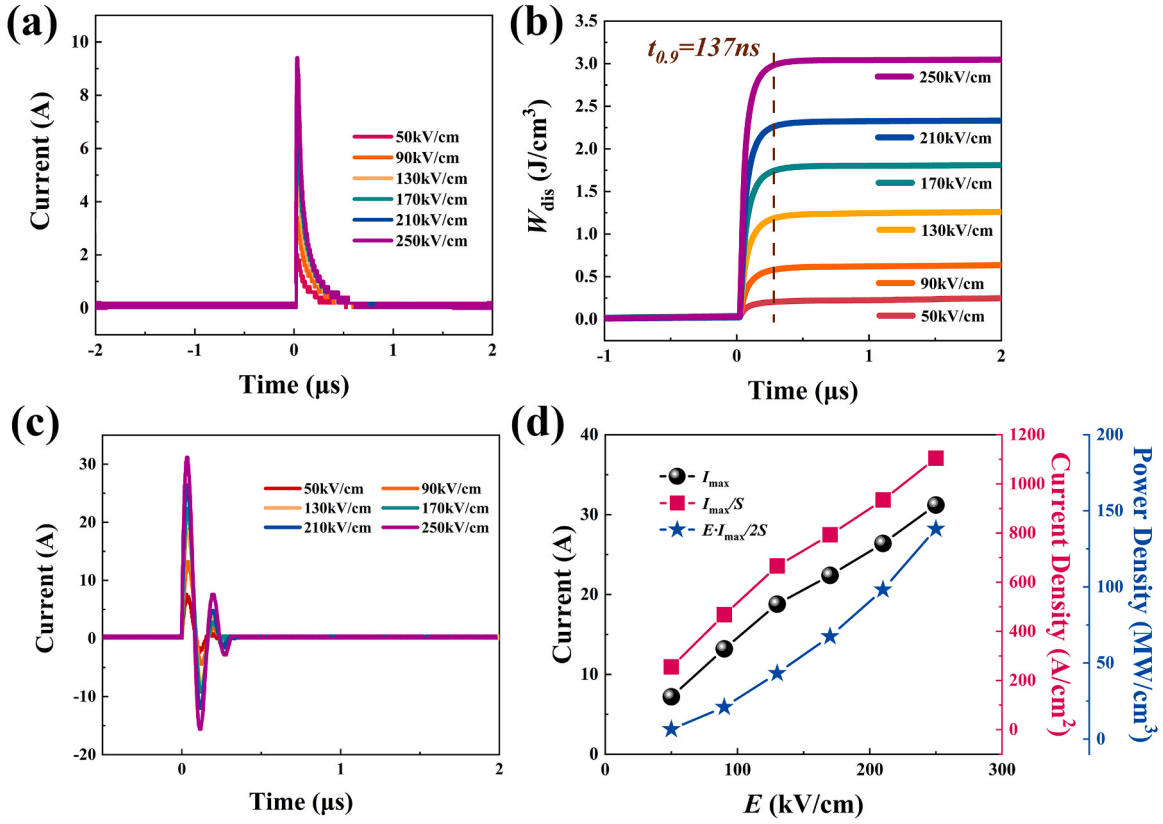

Fig. 13. The pulse characteristics of 0.30SBT (VPP) ceramics at room temperature.

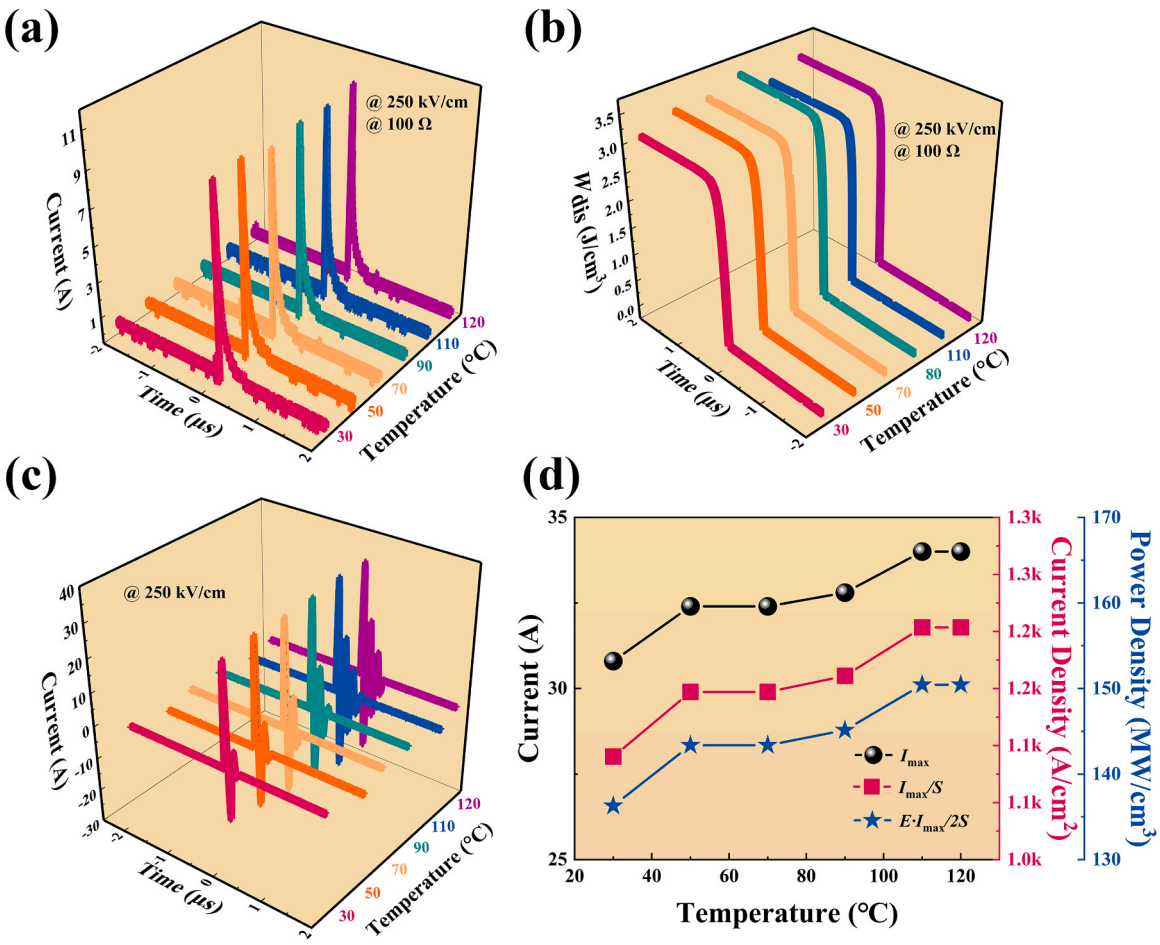

Fig. 14. The temperature-dependent pulse characteristics of 0.30SBT (VPP) ceramics.

0.30SBT ceramics has been elucidated. In summary, this study provides a reliable example for designing lead-free relaxor ferroelectric ceramics to achieve desired energy storage behavior.

CRediT authorship contribution statement

Gang Liu: Resources, Project administration, Formal analysis, Data curation, Conceptualization. **Yan Yan:** Software, Project administration, Formal analysis, Data curation. **Minghui Hao:** Writing – review & editing, Visualization, Conceptualization. **Minghui He:** Software, Methodology, Investigation. **Yang He:** Visualization, Resources, Data curation, Conceptualization. **Xinyu Chen:** Supervision, Software, Formal analysis, Conceptualization. **Alexander N. Vtyurin:** Visualization, Software, Methodology, Formal analysis. **Chunlin Song:** Writing – review & editing, Writing – original draft, Methodology, Funding acquisition, Formal analysis, Data curation, Conceptualization. **Meng Qi:** Visualization, Methodology, Formal analysis. **Yuxiang He:** Visualization, Supervision, Project administration. **Xinyu Liu:** Writing – review & editing, Writing – original draft, Visualization, Validation, Supervision, Software, Resources, Project administration, Funding acquisition, Data curation, Conceptualization. **Weiping Gong:** Software, Project administration, Investigation, Formal analysis. **Taotao Ai:** Validation, Supervision, Resources, Data curation, Conceptualization. **Qin Li:** Writing – original draft, Software, Methodology, Data curation, Conceptualization. **Ting Wang:** Resources, Investigation, Conceptualization.

Declaration of Competing Interest

The authors declare that they have no known competing financial interests or personal relationships that could have appeared to influence the work reported in this paper.

Data Availability

No data was used for the research described in the article.

Acknowledgements

The authors thanks to the sponsorship of the National Natural Science Foundation of China (52372126, 52073235, 52172130), Guangdong Provincial Key Laboratory of Electronic Functional Materials and Devices (EFMD2022001Z), the Natural Science Basic Research Program of Shaanxi (Program No. 2024JC-ZDXM-32) and the Natural Science Foundation of Chongqing, China (CSTB2022NSCQ-MSX0455).

References

[1] F.Z. Yao, Q. Yuan, Q. Wang, H. Wang, Multiscale structural engineering of dielectric ceramics for energy storage applications: from bulk to thin films, Nanoscale 12 (2020) 17165–17184.
[2] G. Ren, G. Ma, N. Cong, Review of electrical energy storage system for vehicular applications, Renew. Sustain. Energy Rev. 41 (2015) 225–236.
[3] K. Yao, S. Chen, M. Rahimabady, M.S. Mirshekarloo, S. Yu, F.E.H. Tay, T. Sritharan, L. Lu, Nonlinear Dielectric Thin Films for High-Power Electric Storage With Energy Density Comparable With Electrochemical Supercapacitors, Ieee Trans. Ultrason. Ferroelectr. Freq. Control 58 (2011) 1968–1974.
[4] M.S. Whittingham, Materials challenges facing electrical energy storage, MRS Bull. 33 (2011) 411–419.

[5] Q. Li, K. Han, M.R. Gadinski, G. Zhang, Q. Wang, High energy and power density capacitors from solution-processed ternary ferroelectric polymer nanocomposites, Adv. Mater. 26 (2014) 6244–6249.

[6] H. Palneedi, M. Peddigari, G.-T. Hwang, D.-Y. Jeong, J. Ryu, High-performance dielectric ceramic films for energy storage capacitors: progress and outlook, Adv. Funct. Mater. 28 (2018).

[7] F. Yan, H. Bai, X. Zhou, G. Ge, G. Li, B. Shen, J. Zhai, Realizing superior energy storage properties in lead-free ceramics via a macro-structure design strategy, J. Mater. Chem. A 8 (2020) 11656–11664.

[8] P. Chen, L.Y. Zhang, J. Cai, Z.Y. Wang, W.J. Shi, J.Y. Jing, F.B. Wei, G. Liu, Y. Yan, H.B. Liu, L. Jin, Effect of Dy_2O_3 content on the dielectric, ferroelectric, and energy storage properties of lead-free $0.5Na_{0.5}Bi_{0.5}TiO_3$-$0.5SrTiO_3$ bulk ceramics, J. Mater. Sci. Mater. Electron. 30 (2019) 13556–13566.

[9] D. Wang, Z. Fan, W. Li, D. Zhou, A. Feteira, G. Wang, S. Murakami, S. Sun, Q. Zhao, X. Tan, I.M. Reaney, High energy storage density and large strain in Bi$(Zn_{2/3}Nb_{1/3})O_3$-Doped $BiFeO_3$-$BaTiO_3$ ceramics, ACS Appl. Energy Mater. 1 (2018) 4403–4412.

[10] R. Ranjan, V. Kothai, R. Garg, A. Agrawal, A. Senyshyn, H. Boysen, Degenerate rhombohedral and orthorhombic states in Ca-substituted $Na_{0.5}Bi_{0.5}TiO_3$, Appl. Phys. Lett. 95 (2009).

[11] M. Chen, Y. Pu, L. Zhang, Novel NBT-based relaxor ferroelectric ceramics with excellent discharge performance and high-temperature stability, J. Mater. Sci. Mater. Electron. 32 (2021) 23540–23553.

[12] X. Liu, B. Liu, F. Li, P. Li, J. Zhai, B. Shen, Relaxor phase evolution and temperature-insensitive large strain in B-site complex ions modified NBT-based lead-free ceramics, J. Mater. Sci. 53 (2017) 309–322.

[13] J. Wang, T. Li, X. Jiang, C. Zhou, Y. Xu, R. Shi, L. Liu, B. Chu, Z. Zhao, R. Zuo, An alternative way to design excellent energy-storage properties in $Na_{0.5}Bi_{0.5}TiO_3$-based lead-free system by constructing relaxor dielectric composites, J. Eur. Ceram. Soc. 42 (2022) 6512–6517.

[14] G. Wang, D.A. Hall, T.P. Comyn, L. Daniel, A.K. Kleppe, Structure and ferroelectric behaviour of $Na_{0.5}Bi_{0.5}TiO_3$-$KNbO_3$ceramics, Adv. Appl. Ceram. 115 (2016) 89–95.

[15] G. Shirane, H. Danner, A. Pavlovic, R. Pepinsky, Phase Transitions in Ferroelectric $KNbO_3$, Phys. Rev. 93 (1954) 672–673.

[16] K. Pengpat, P. Jarupoom, P. Kantha, S. Eitssayeam, U. Intatha, G. Rujijanagul, T. Tunkasiri, Phase formation and electrical properties of lead-free bismuth sodium titanate–potassium niobate ceramics, Curr. Appl. Phys. 8 (2008) 241–245.

[17] Y. Guo, K.-i Kakimoto, H. Ohsato, Structure and Electrical Properties of Lead-Free $(Na_{0.5}K_{0.5})NbO_3$-$BaTiO_3$ Ceramics, Jpn J. Appl. Phys. 43 (2004) 2008.

[18] S. Tashiro, H. Nagamatsu, K. Nagata, Sinterability and piezoelectric properties of $KNbO_3$ ceramics after substituting Pb and Na for K, Jpn. J. Appl. Phys. Part 1-Regul. Pap. Short. Notes Rev. Pap. 41 (2002) 7113–7118.

[19] R. Duan, J. Wang, S. Jiang, H. Cheng, J. Li, A. Song, B. Hou, D. Chen, Y. Liu, Impact of La doping on performance of $Na_{0.5}Bi_{0.5}TiO_3$-$Ba_{0.7\text{-}x}La_xSr_{0.3}Sn_{0.1}Ti_{0.9\text{-}0.25x}O_3$ dielectric ceramics, J. Alloy. Compd. 745 (2018) 121–126.

[20] Y. Jiao, S. Song, F. Chen, X. Zeng, X. Wang, C. Song, G. Liu, Y. Yan, Energy storage performance of $0.55Bi_{0.5}Na_{0.5}TiO_3$-$0.45SrTiO_3$ ceramics doped with lanthanide elements (Ln = La, Nd, Dy, Sm) using a viscous polymer processing route, Ceram. Int. 48 (2022) 10885–10894.

[21] X. Zhang, L. Zhao, L. Liu, Za Zhang, B. Cui, Interface and defect modulation via a core–shell design in $(Na_{0.5}Bi_{0.5}TiO_3$-$La_2O_3)$-$(SrSn_{0.2}Ti_{0.8}O_3$-$La_2O_3)$-Bi_2O_3-B_2O_3-SiO_2 composite ceramics for wide-temperature energy storage capacitors, Chem. Eng. J. 435 (2022) 135061.

[22] G. Liu, L. Hu, Y. Wang, Z. Wang, L. Yu, J. Lv, J. Dong, Y. Wang, M. Tang, B. Guo, K. Yu, Y. Yan, Investigation of electrical and electric energy storage properties of La -doped $Na_{0.3}Sr_{0.4}Bi_{0.3}TiO_3$ based Pb-free ceramics, Ceram. Int. 46 (2020) 19375–19384.

[23] Q. Li, X. Liu, F. Chen, L. Yang, M. He, M. Qi, Y. He, C. Tian, X. Zhao, H. Tang, K. Yu, G. Liu, Y. Zhao, X. Liu, Y. Yan, Achieving improved dielectric energy storage properties and temperature stability in $0.91Na_{0.5}Bi_{0.5}TiO_3$-$0.09K_{0.7}La_{0.1}NbO_3$ based ferroelectric ceramics by composition design and processing optimization, Ceram. Int. 50 (2024) 18945–18957.

[24] M.A. Khan, A. Manan, M. Ur Rehman, S. Faisal, A.H. Shah, H.U. Shah, F. Alresheedi, Z.A. Ghazi, S.U. Khan, Enhanced energy storage characteristics of Bi$(Mg_{0.5}Ce_{0.5})O_3$ modified $(Sr_{0.7}Bi_{0.2})TiO_3$ lead-free ceramics, J. Mater. Eng. Perform. 33 (2023) 1538–1547.

[25] M.A. Khan, A. Manan, M.U. Rehman, S.U. Khan, S. Faisal, A.H. Wazir, F. Alresheedi, M.T. Lanagan, $K_{0.5}Bi_{0.5})(Mg_{1/3}Nb_{2/3})O_3$-modified $Sr_{0.7}Bi_{0.2}TiO_3$ lead-free ceramics for energy storage applications, Int. J. Appl. Ceram. Technol. 21 (2023) 947–956.

[26] J. Wang, T. Li, C. Zhou, A. Rahman, D. Chen, X. Jiang, A. Xie, H. Ma, X. Fang, Z. Yang, H. Zheng, R. Zuo, Achieving high energy storage density under low electric field in modified bismuth sodium titanate ceramics, J. Mater. Sci. Mater. Electron. 34 (2023).

[27] J. Wang, C. Zhou, Q. Li, W. Zeng, J. Xu, G. Chen, C. Yuan, G. Rao, Dual relaxation behaviors and large electrostrictive properties of $Bi_{0.5}Na_{0.5}TiO_3$-$Sr_{0.85}Bi_{0.1}TiO_3$ ceramics, J. Mater. Sci. 53 (2018) 8844–8854.

[28] X. Liu, J. Shi, F. Zhu, H. Du, T. Li, X. Liu, H. Lu, Ultrahigh energy density and improved discharged efficiency in bismuth sodium titanate based relaxor ferroelectrics with A-site vacancy, J. Mater. 4 (2018) 202–207.

[29] C. Wu, X. Qiu, L. Chen, C. Liu, H. Zhao, W. Ge, Z. Liu, M. Yao, A strategy to achieve high energy storage performance under a relatively low electric field in NBT-based ceramics, J. Alloy. Compd. 910 (2022) 164851.

[30] M. Chen, S. Zhan, Q. Yuan, Y. Li, Y. Lin, H. Yang, Enhanced energy storage performance of $Na_{0.5}Bi_{0.5}TiO_3$ lead-free ceramics under low electric field, Mater. Today Energy 31 (2023) 101193.

[31] J. Lv, Q. Li, Y. Li, M. Tang, D. Jin, Y. Yan, B. Fan, L. Jin, G. Liu, Significantly improved energy storage performance of NBT-BT based ceramics through domain control and preparation optimization, Chem. Eng. J. 420 (2021) 129900.

[32] W. Wang, L. Zhang, Y. Yang, W. Shi, Y. Huang, D.O. Alikin, V.Y. Shur, Z. Lou, A. Zhang, X. Wei, D. Wang, F. Gao, H. Du, L. Jin, Enhancing energy storage performance in $Na_{0.5}Bi_{0.5}TiO_3$-based lead-free relaxor ferroelectric ceramics along a stepwise optimization route, J. Mater. Chem. A 11 (2023) 2641–2651.

[33] B. Su, T.W. Button, A comparative study of viscous polymer processed ceramics based on aqueous and non-aqueous binder systems, J. Mater. Process Technol. 209 (2009) 153–157.

[34] K. Yao, C. Zhou, J. Wang, Q. Li, C. Yuan, J. Xu, G. Chen, G. Rao, A new strategy to realize high energy storage properties and ultrafast discharge speed in $Sr_{0.7}Bi_{0.2}TiO_3$-based relaxor ferroelectric ceramic, J. Alloy. Compd. 883 (2021).

[35] L. Venkidu, D.E. Jain Ruth, M. Veera Gajendra Babu, P. Esther Rubavathi, D. Dhayanithi, N.V. Giridharan, B. Sundarakannan, Suppression of intermediate antiferroelectric phase in sub-micron grain size $Na_{0.5}Bi_{0.5}TiO_3$ ceramics, J. Mater. Sci. Mater. Electron. 33 (2022) 25006–25024.

[36] L. Zhang, Y. Pu, M. Chen, F. Zhuo, C. Dietz, T. Frömling, Decreasing polar-structure size: Achieving superior energy storage properties and temperature stability in $Na_{0.5}Bi_{0.5}TiO_3$-based ceramics for low electric field and high-temperature applications, J. Eur. Ceram. Soc. 41 (2021) 5890–5899.

[37] N. Luo, K. Han, F. Zhuo, L. Liu, X. Chen, B. Peng, X. Wang, Q. Feng, Y. Wei, Design for high energy storage density and temperature-insensitive lead-free antiferroelectric ceramics, J. Mater. Chem. C. 7 (2019) 4999–5008.

[38] G. Liu, Y. Li, Z. Wang, L. Zhang, P. Chen, F. Wei, Y. Wang, K. Yu, Y. Yan, L. Jin, Z. He, Dielectric, ferroelectric and energy storage properties of lead-free $(1\text{-}x)$ $Ba_{0.9}Sr_{0.1}TiO_3$-$xBi(Zn_{0.5}Zr_{0.5})O_3$ ferroelectric ceramics sintered at lower temperature, Ceram. Int. 45 (2019) 15556–15565.

[39] I.-R. Yoo, S.-H. Choi, J.-Y. Park, M.-S. Kim, A.K. Yadav, K.-H. Cho, A superparaelectric state in relaxor ferroelectric (Sr,Bi)TiO_3-Bi(Mg,Ti)O_3-Modified $BaTiO_3$ ceramics to achieve high energy storage performance, Materials 17 (2024).

[40] A.K. Yadav, I.-R. Yoo, S.-H. Choi, J.-Y. Park, M.-S. Kim, J. Cho, H.-C. Song, K.-H. Cho, Enhanced energy storage and temperature-stable dielectric properties in $(1\text{-}x)[(Na_{0.4}K_{0.1}Bi_{0.5})_{0.94}Ba_{0.06}TiO_3]$-$xLa_{0.2}Sr_{0.7}TiO_3$ lead-free relaxor ceramics, J. Alloy. Compd. 985 (2024).

[41] H. He, W. Lu, J.A.S. Oh, Z. Li, X. Lu, K. Zeng, L. Lu, Probing the coexistence of ferroelectric and relaxor states in $Bi_{0.5}Na_{0.5}TiO_3$-based ceramics for enhanced piezoelectric performance, ACS Appl. Mater. Interfaces 12 (2020) 30548–30556.

[42] M. Habib, F. Akram, P. Ahmad, I. Kebaili, A. Rahman, I.U. Din, M.J. Iqbal, A. Zeb, M.U. Khandaker, A. Karoui, M.-H. Kim, T.K. Song, Ultrahigh piezoelectric strain in lead-free $BiFeO_3$-$BaTiO_3$ ceramics at elevated temperature, J. Alloy. Compd. 919 (2022).

[43] D.E. Jain Ruth, B. Sundarakannan, Structural and Raman spectroscopic studies of poled lead-free piezoelectric sodium bismuth titanate ceramics, Ceram. Int. 42 (2016) 4775–4778.

[44] R. Roukos, N. Zaiter, D. Chaumont, Relaxor behaviour and phase transition of perovskite ferroelectrics-type complex oxides $(1\text{–}x)Na_{0.5}Bi_{0.5}TiO_3$–$xCaTiO_3$ system, J. Adv. Ceram. 7 (2018) 124–142.

[45] C. Ma, X. Tan, H.J. Kleebe, In situ transmission electron microscopy study on the phase transitionsin lead-free $(1-x)(Bi_{1/2}Na_{1/2})TiO_3$–$x$$BaTiO_3$ ceramics, J. Am. Ceram. Soc. 94 (2011) 4040–4044.

[46] A. Singha, S. Praharaj, S.K. Rout, D. Rout, Composition dependent crossover from ferroelectric to relaxor-ferroelectric in NBT-ST-KNN ceramics, Curr. Appl. Phys. 36 (2022) 160–170.

[47] D. Rout, K.-S. Moon, J. Park, S.-J.L. Kang, High-temperature X-ray diffraction and Raman scattering studies of Ba-doped $(Na_{0.5}Bi_{0.5})TiO_3$ Pb-free piezoceramics, Curr. Appl. Phys. 13 (2013) 1988–1994.

[48] K. Datta, A. Richter, M. Göbbels, R.B. Neder, B. Mihailova, Atomistic origin of huge response functions at the morphotropic phase boundary of$(1-x)$ $Na_{0.5}Bi_{0.5}TiO_3-xBaTiO_3$, Phys. Rev. B 90 (2014).

[49] G. Liu, L. Zhang, Z. Wang, W. Jiang, J. Cai, X. Liu, Y. Chen, C. Song, Y. Yan, The doping effects of $ZnNb_2O_6$ on the phase, microstructure and energy storage properties of $(Sr_{0.98}Ca_{0.02})TiO_3$ paraelectric ceramics, Ferroelectrics 531 (2018).

[50] A. Prado, J. Camargo, P. Öchsner, L. Ramajo, M. Castro, Synthesis and characterization of $Bi_{0.5}Na_{0.5}TiO_3$-$BaTiO_3$-$K_{0.5}Na_{0.5}NbO_3$ ceramics for energy storage applications, J. Electroceram. 44 (2020) 248–255.

[51] F. Naeem, M. Saleem, H. Jabbar, G. Tanvir, F. Asif, A.H. Baluch, M. Irfan, A. Ghaffar, A. Maqbool, T. Rafiq, Enhanced ferroelectric and dielectric properties of niobium-doped lead-free piezoceramics, Mater. (Basel) 16 (2023) 477.

[52] A.A. Kamal, H.Y. Morshidy, A. Salem, A.E.-r Mahmoud, The effect of domain switching on the lattice symmetry and dielectric properties of $(Bi_{0.5}Na_{0.3}K_{0.2})$ TiO_3–$0.2SrTiO_3$-$(Ba_{0.8}Ca_{0.2})TiO_3$ piezo-ceramic by poling field, Mater. Chem. Phys. 288 (2022) 126420.

[53] C. Wu, X. Qiu, W. Ge, C. Liu, H. Zhao, L. Chen, Z. Liu, L. Li, J.G. Fisher, Enhanced energy storage performance and temperature stability achieved by a synergic effect in Nd^{3+}/Ga^{3+} co-doped $(Na_{0.5}Bi_{0.5})TiO_3$ -based ceramics, Ceram. Int. 48 (2022) 31931–31940.

[54] X. Zhang, F. Yang, W. Miao, Z. Su, J. Zhao, L. Tang, Y. Shen, D. Hu, Y. Chen, P. Li, J. Liu, Z. Pan, Effective improved energy storage performances of $Na_{0.5}Bi_{0.5}TiO_3$-based relaxor ferroelectrics ceramics by A/B-sites co-doping, J. Alloy. Compd. 883 (2021).

[55] Z. Cai, X. Wang, W. Hong, B. Luo, Q. Zhao, L. Li, Grain-size-dependent dielectric properties in nanograin ferroelectrics, J. Am. Ceram. Soc. 101 (2018) 5487–5496.
[56] D. Hu, Z. Pan, X. Zhang, H. Ye, Z. He, M. Wang, S. Xing, J. Zhai, Q. Fu, J. Liu, Greatly enhanced discharge energy density and efficiency of novel relaxation ferroelectric BNT-BKT-based ceramics, J. Mater. Chem. C. 8 (2020) 591–601.
[57] J. Wu, X. Wang, X. Cheng, T. Zheng, B. Zhang, D. Xiao, J. Zhu, X. Lou, New potassium-sodium niobate lead-free piezoceramic: Giant-d_{33} vs. sintering temperature, J. Appl. Phys. 115 (2014) 114104.
[58] D. You, H. Tan, Z. Yan, H. Gao, S. Chen, W. Ma, P. Fan, N.-M.-A. Tran, Y. Liu, D. Salamon, H. Zhang, Enhanced Dielectric Energy Storage Performance of 0.45$Na_{0.5}Bi_{0.5}TiO_3$-0.55$Sr_{0.7}Bi_{0.2}TiO_3$/AlN 0-3 Type Lead-Free Composite Ceramics, ACS Appl. Mater. Interfaces 14 (2022) 17652–17661.
[59] M.M. Costa, G.F.M. Pires, A.J. Terezo, M.P.F. Graça, A.S.B. Sombra, Impedance and modulus studies of magnetic ceramic oxide $Ba_2Co_2Fe_{12}O_{22}$ (Co_2Y) doped with Bi_2O_3, J. Appl. Phys. 110 (2011).
[60] A.K. Jonscher, A new understanding of the dielectric relaxation of solids, J. Mater. Sci. 16 (1981) 2037–2060.
[61] W. Wang, Y. Pu, X. Guo, R. Shi, Y. Shi, M. Yang, J. Li, X. Peng, Y. Li, Enhanced energy storage density and high efficiency of lead-free $Ca_{1-x}SrTi_{1-y}ZrO_3$ linear dielectric ceramics, J. Eur. Ceram. Soc. 39 (2019) 5236–5242.
[62] G. Liu, Y. Wang, G. Han, J. Gao, L. Yu, M. Tang, Y. Li, J. Hu, L. Jin, Y. Yan, Enhanced electrical properties and energy storage performances of NBT-ST Pb-free ceramics through glass modification, J. Alloy. Compd. 836 (2020).
[63] H. Qi, R. Zuo, X. Zhou, D. Zhang, Phase structure dependence of acceptor doping effects in $(Bi_{0.5}Na_{0.5})TiO_3$–$BaTiO_3$ lead-free ceramics, J. Alloy. Compd. 802 (2019) 6–12.
[64] H. Luo, H. Qi, S. Sun, L. Wang, Y. Ren, H. Liu, S. Deng, J. Chen, Structural origin for the high piezoelectric performance of $(Na_{0.5}Bi_{0.5})TiO_3$-$BaTiO_3$-$BiAlO_3$ lead-free ceramics, Acta Mater. 218 (2021) 117202.
[65] X. Liu, X. Tan, Giant strains in non-textured $(Bi_{1/2}Na_{1/2})TiO_3$-based lead-free ceramics, Adv. Mater. 28 (2015) 574–578.
[66] J.-S. Park, C.-J. Jeon, Y.-H. Jeong, J.-S. Yun, J.-H. Cho, Crystal structures and domain patterns of unpoled and poled $Bi_{0.5}(Na_{0.78}K_{0.22})_{0.5}TiO_3$ ceramics by TEM, Mater. Lett. 167 (2016) 218–221.
[67] S. Lu, Z. Xu, R. Zuo, Comparative study of the effect of domain structures on piezoelectric properties in three typical Pb-free piezoceramics, Ceram. Int. 40 (2014) 13565–13571.
[68] J. Lv, S. Song, Y. Jiao, Z. Yang, Y. Zhang, Y. Fan, C. Song, G. Liu, Enhancing the dielectric and energy storage properties of lead-free $Na_{0.5}Bi_{0.5}TiO_3$–$BaTiO_3$ ceramics by adding $K_{0.5}Na_{0.5}NbO_3$ ferroelectric, Ceram. Int. 48 (2022) 22–31.
[69] T. Wang, L. Zhang, A. Zhang, J. Liu, L. Kong, G. Chen, Y. Cheng, Y. Tian, H. Yang, Y. Hu, Z. Xing, C. Li, L. Jin, Synergistic enhanced energy storage performance of NBT-KBT ceramics by $K_{0.5}Na_{0.5}NbO_3$ composition design, J. Alloy. Compd. 948 (2023) 169725.
[70] Z. Ling, J. Ding, W. Miao, J. Liu, J. Zhao, L. Tang, Y. Shen, Y. Chen, P. Li, Z. Pan, MnO_2-modified lead-free NBT-based relaxor ferroelectric ceramics with improved energy storage performances, Ceram. Int. 47 (2021) 22065–22072.
[71] M. Li, P. Fan, W. Ma, K. Liu, J. Zang, C. Samart, T. Zhang, H. Tan, D. Salamon, H. Zhang, Constructing layered structures to enhance the breakdown strength and energy density of $Na_{0.5}Bi_{0.5}TiO_3$-based lead-free dielectric ceramics, J. Mater. Chem. C. 7 (2019) 15292–15300.
[72] X. Liu, Y. Hou, Y. Xu, M. Zheng, M. Zhu, Realization of temperature insensitive high energy storage performance via introducing $NaNbO_3$ into NBT-KBT system, J. Alloy. Compd. 844 (2020) 156163.
[73] L. Zhang, Y. Pu, M. Chen, R. Li, X. Guo, Y. Cui, Enhanced energy-storage properties of (1-x)$Na_{0.5}Bi_{0.5}TiO_3$-$x$$BaSnO_3$ ceramics, Ceram. Int. 44 (2018) S207–S210.
[74] K. Wang, W. Li, X. Tang, S. Zhang, Y. Zhang, J. Hu, Z. Shen, Y. Jiang, X. Guo, High recoverable energy storage density of $Na_{0.5}Bi_{0.5}TiO_3$ lead-free ceramics modified by $Bi(Mg_{0.5}Hf_{0.5})O_3$, J. Adv. Dielectr. 13 (2023) 2350008.
[75] W. Qin, M. Zhao, Z. Li, D. Zhang, M. Zhang, Y. Xu, L. Jin, Y. Yan, High energy storage and thermal stability under low electric field in $Bi_{0.5}Na_{0.5}TiO_3$-modified $BaTiO_3$-$Bi(Zn_{0.25}Ta_{0.5})O_3$ ceramics, Chem. Eng. J. 443 (2022) 136505.
[76] C. Ma, R. Zhang, G. Zhang, H. Du, J. Liu, R. Liang, Z. Wang, Structural evolution and energy storage properties of $Bi(Zn_{0.5}Zr_{0.5})O_3$ modified $BaTiO_3$-based relaxation ferroelectric ceramics, J. Energy Storage 72 (2023) 108374.
[77] C. Ma, R. Zhang, G. Zhang, H. Du, J. Liu, R. Liang, Z. Wang, Effect of $Bi(Zn_{1/2}Nb_{2/5})O_3$ addition on phase transition and energy storage properties of $BaTiO_3$ ceramics, Curr. Appl. Phys. 55 (2023) 1–8.
[78] D. Meng, Q. Feng, N. Luo, C. Yuan, C. Zhou, Y. Wei, T. Fujita, H. You, G. Chen, Effect of $Sr(Zn_{1/3}Nb_{2/3})O_3$ modification on the energy storage performance of $BaTiO_3$ ceramics, Ceram. Int. 47 (2021) 12450–12458.
[79] Y. Li, M.-Y. Tang, Z.-G. Zhang, Q. Li, J.-L. Li, Z. Xu, G. Liu, F. Li, $BaTiO_3$-based ceramics with high energy storage density, Rare Met. 42 (2023) 1261–1273.
[80] P.-Z. Ge, Z.-G. Liu, X.-X. Huang, X.-G. Tang, Z.-H. Tang, S.-F. Li, Q.-X. Liu, Y.-P. Jiang, X.-B. Guo, Excellent energy storage properties realized in novel $BaTiO_3$-based lead-free ceramics by regulating relaxation behavior, J. Mater. 9 (2023) 910–919.
[81] Q. Jin, E. Song, K. Cai, Enhanced Energy Storage Performance of Lead-Free $BaTiO_3$-$K_{0.5}Na_{0.5}NbO_3$ via Grain Engineering, J. Electron. Mater. 51 (2022) 5188–5204.
[82] T. Wang, J. Liu, L. Kong, H. Yang, F. Wang, C. Li, Evolution of the structure, dielectric and ferroelectric properties of $Na_{0.5}Bi_{0.5}TiO_3$-added $BaTiO_3$-$Bi(Mg_{2/3}Nb_{1/3})O_3$ ceramics, Ceram. Int. 46 (2020) 25392–25398.
[83] S. Liu, W. Feng, J. Li, B. Tang, C. Hu, Y. Zhong, B. He, D. Luo, Achieving excellent energy storage performance at moderate electric field in $Ca_{0.85}Bi_{0.05}Sm_{0.05}TiO_3$-modified $BiFeO_3$-based relaxor ceramics via multiple synergistic design, Chem. Eng. J. 470 (2023) 144086.
[84] A. Jain, A. Kumar, N. Gupta, Significant Improvement in Magnetic and Magnetoelectric Characteristics of (0.95−x)$Ba_{0.9}Ca_{0.1}TiO_3$-0.05$Na_{0.5}Bi_{0.5}TiO_3$-$x$$CoFe_2O_4$ ceramics, IEEE Trans. Magn. 58 (2022) 1–14.
[85] A. Jain, Y. Wang, H. Guo, N. Wang, Grain size engineered $Ba_{0.9}Sr_{0.1}Ti_{0.9}Hf_{0.1}O_3$-$Na_{0.5}Bi_{0.5}TiO_3$ relaxor ceramics with improved energy storage performance, J. Am. Ceram. Soc. 103 (2020) 6308–6318.
[86] R. Zhang, L. Zhao, Za Zhang, X. Zhang, Q. Jin, B. Cui, Boosting energy storage performance in $Ba_{0.8}Sr_{0.2}Zr_{0.1}Ti_{0.9}O_3$–$Na_{0.5}Bi_{0.5}TiO_3$ lead-free nanoceramics through polar nanoregions and grain refinement engineering, J. Mater. Sci. Mater. Electron. 32 (2021) 7259–7270.
[87] Y.-S. Zhang, W.-H. Li, X.-G. Tang, K. Meng, S.-Y. Zhang, X.-Z. Xiao, X.-B. Guo, Y.-P. Jiang, Z. Tang, Energy storage and charge-discharge performance of B-site doped NBT-based lead-free ceramics, J. Alloy. Compd. 911 (2022).
[88] X. Zhang, W. Xia, Y. Chen, Y. Liang, Effect of $K_{0.5}Bi_{0.5}TiO_3$ on energy storage properties and temperature stability of $Bi_{0.5}Na_{0.5}TiO_3$-$Bi_{0.2}Sr_{0.7}TiO_3$ ceramics, J. Electroceram. 51 (2023) 80–89.
[89] Q. Feng, C. Yuan, X. Liu, S. Wu, G. Chen, Q. Li, C. Zhou, J. Xu, F. Liu, Microstructures and energy-storage properties of (1−x)$(Na_{0.5}Bi_{0.5})TiO_3$–$x$$BaTiO_3$ with BaO–B_2O_3–SiO_2 additions, J. Mater. Sci. Mater. Electron. 26 (2015) 5113–5119.
[90] Z. He, S. Shi, Z. Pan, L. Tang, J. Zhao, Y. Shen, D. Hu, Y. Chen, P. Li, J. Liu, J. Zhai, Low electric field induced high energy storage capability of the free-lead relaxor ferroelectric 0.94$Bi_{0.5}Na_{0.5}TiO_3$-0.06$BaTiO_3$-based ceramics, Ceram. Int. 47 (2021) 11611–11617.
[91] H. Li, S. Zhou, J. Zhao, T. Yan, Y. Du, H. Zhou, Y. Pu, D. Wang, Dielectric temperature stability and energy storage performance of NBT-based lead-free ceramics for Y9P capacitors, J. Adv. Dielectr. 13 (2022).
[92] H. Yang, J. Tian, Y. Lin, J. Ma, Realizing ultra-high energy storage density of lead-free 0.76$Bi_{0.5}Na_{0.5}TiO_3$-0.24$SrTiO_3$-$Bi(Ni_{2/3}Nb_{1/3})O_3$ ceramics under low electric fields, Chem. Eng. J. 418 (2021).
[93] W. Cao, L. Li, H. Zhao, C. Wang, C. Liang, F. Li, X. Huang, C. Wang, Outstanding energy storage performance of NBT-based ceramics under moderate electric field achieved via antiferroelectric engineering, ACS Appl. Mater. Interfaces 15 (2023) 38633–38643.
[94] A. Zhang, T. Wang, J. Liu, J. Liu, G. Chen, H. Yang, L. Kong, Y. Cheng, Y. Tian, C. Li, L. Jin, Significant improvement in energy storage for BT ceramics via NBT composition regulation, J. Alloy. Compd. 968 (2023).
[95] Y.C. Wu, Y.Z. Fan, N.T. Liu, P. Peng, M.X. Zhou, S.G. Yan, F. Cao, X. Dong, G. S. Wang, Enhanced energy storage properties in sodium bismuth titanate- based ceramics for dielectric capacitor applications, J. Mater. Chem. C. 7 (2019) 6222–6230.
[96] M. Qi, H. Feng, M. He, F. Chen, Y. He, Q. Li, L. Yang, Y. Zheng, D. Meng, X. Zhao, Y. Yan, L. Zhang, L. Jin, C. Song, G. Liu, Enhanced energy storage performance in Pb-free $Na_{0.5}Bi_{0.5}TiO_3$–$Sr_{0.7}Bi_{0.2}TiO_3$-based relaxor ferroelectric ceramics through a stepwise optimization strategy, Ceram. Int. 50 (2024) 30051–30060.
[97] L.-F. Zhu, A. Song, B.-P. Zhang, X.-Q. Gao, Z.-H. Shan, G.-L. Zhao, J. Yuan, D. Deng, H. Shu, J.-F. Li, Boosting energy storage performance of $BiFeO_3$-based multilayer capacitors via enhancing ionic bonding and relaxor behavior, J. Mater. Chem. A 10 (2022) 7382–7390.
[98] R. Montecillo, C.Y. Chen, R.F.G. Sinajon, Y.-T. Lee, R.R. Chien, K.-C. Feng, P.-Y. Chen, C.-S. Chen, C.-S. Tu, Optimizing energy storage under low electric field in A-site dysprosium modified $BiFeO_3$-$BaTiO_3$ ceramics, J. Alloy. Compd. 983 (2024).
[99] C.-S. Chen, Z.-Q. Lin, R. Montecillo, J.-Y. Liao, P.-Y. Chen, C.-S. Tu, Improved energy storage in antiferroelectric $AgNbO_3$-modulated 0.925$Bi_{0.5}Na_{0.5}TiO_3$ – 0.075$BaTiO_3$ relaxor ferroelectric ceramics, Ceram. Int. 48 (2022) 35452–35460.
[100] S.-Y. Chen, R. Montecillo, K.-C. Feng, R.R. Chien, P.-Y. Chen, C.-S. Chen, C.-S. Tu, High-efficiency energy storage in Nd-doped (1-x)$BiFeO_3$–$x$$BaTiO_3$ relaxor ferroelectric ceramics, Ceram. Int. 49 (2023) 26625–26634.
[101] R. Montecillo, J.-C. Lin, C.-S. Chen, P.-Y. Chen, C.-S. Tu, Tailoring energy storage in Nb_2O_5-added 0.7$BiFeO_3$–0.3$BaTiO_3$ ceramics via A-site Gd^{3+} substitution, J. Alloy. Compd. 963 (2023).
[102] H. Sun, X. Wang, Q. Sun, X. Zhang, Z. Ma, M. Guo, B. Sun, X. Zhu, Q. Liu, X. Lou, Large energy storage density in $BiFeO_3$-$BaTiO_3$-$AgNbO_3$ lead-free relaxor ceramics, J. Eur. Ceram. Soc. 40 (2020) 2929–2935.
[103] R. Montecillo, C.-S. Chen, K.-C. Feng, R.R. Chien, S.-C. Haw, P.-Y. Chen, C.-S. Tu, Achieving superb electric energy storage in relaxor ferroelectric $BiFeO_3$-$BaTiO_3$-$NaNbO_3$ ceramics via O_2 atmosphere, J. Eur. Ceram. Soc. 43 (2023) 7446–7454.
[104] R. Montecillo, C.-S. Chen, K.-C. Feng, R.R. Chien, P.-Y. Chen, C.-S. Tu, Configuration-entropy effects on $BiFeO_3$–$BaTiO_3$ relaxor ferroelectric ceramics for high-density energy storage, J. Mater. Chem. A 12 (2024) 11995–12008.
[105] Z.B. Pan, D. Hu, Y. Zhang, J.J. Liu, B. Shen, J.W. Zhai, Achieving high discharge energy density and efficiency with NBT-based ceramics for application in capacitors, J. Mater. Chem. C. 7 (2019) 4072–4078.
[106] X. Zhou, H. Qi, Z. Yan, G. Xue, H. Luo, D. Zhang, Superior thermal stability of high energy density and power density in domain-engineered $Bi_{0.5}Na_{0.5}TiO_3$-$NaTaO_3$ relaxor ferroelectrics, ACS Appl. Mater. Interfaces 11 (2019) 43107–43115.